

Supplementary Note 5  
(Details of Material Characterization)  
for

**Leveraging Data Mining, Active Learning, and Domain Adaptation  
in a Multi-Stage, Machine Learning-Driven Approach for the  
Efficient Discovery of Advanced Acidic Oxygen Evolution  
Electrocatalysts**

Rui Ding *et al.*

\*Corresponding author. Email: [junhongchen@uchicago.edu](mailto:junhongchen@uchicago.edu), [chenyuxin@uchicago.edu](mailto:chenyuxin@uchicago.edu)

## **Supplementary Note Discussion SND 5-1**

### **Characterization Instruments**

In this work, to further understand the material properties of screened samples, we used different characterization tools for comprehensive materials analysis. The experimental details are as follows:

#### **BET:**

Brunauer–Emmett–Teller (BET) Nitrogen adsorption-desorption isotherms were performed on AUTOSORB IQ (Quantachrome instruments) at 77 K, and the surface areas were fitted by the BET equation.

#### **XRD:**

X-ray Diffraction (XRD) is one of the fundamental tools for compositional and phase analysis of synthesized materials. In this study, XRD measurements were conducted using a Rigaku D/MAX-Ultima III powder diffractometer (Cu-K $\alpha$  radiation, 40 mV, 40 mA,  $\lambda = 0.1542$  nm). The scanning mode and angle range were set to cover from 20° to 80°, with a scanning speed of 10° min $^{-1}$ .

#### **SEM:**

Scanning Electron Microscopy (SEM) is a commonly used method for observing the microstructure of materials. It operates on the principle of collecting secondary electrons emitted from the sample surface under an electron beam, correlating the scanning geometry with morphological information. In this work, SEM analysis was performed on a Regulus8100 equipped with Energy-Dispersive X-ray (EDX) spectroscopy.

#### **TEM:**

Field-Emission Transmission Electron Microscopy (TEM) offers higher resolution compared to SEM, utilizing an electron beam as the light source for the sample. Due to its shorter wavelength, TEM can resolve much smaller structures. With techniques such as spherical aberration correction, TEM can achieve sub-atomic level resolution. In this study, a TECNAT G2 F20 equipped with EDX was used to observe the oxide catalysts and element distribution. The samples for observation were prepared by scooping a small amount of catalyst powder with a spatula, dispersing it in anhydrous ethanol, and then ultrasonically dispersing it. A few drops of the clear dispersion were then placed on an ultra-thin carbon support film and air-dried naturally.

#### **XPS:**

X-ray Photoelectron Spectroscopy (XPS) is primarily used to obtain information about the surface of samples. It operates on the principle of exciting photoelectrons from the surface atoms of the sample using emitted X-ray radiation and analyzing them. In this work, the measurements were conducted on a PHI 5000 VersaProbe spectrometer (ULVAC-PHI). The X-ray source was set to monochromatic Al-K $\alpha$  line (1,486.60 eV). For calibration and comparability of the XPS spectra, the binding energy peak of C1s was set at 284.80 eV and used as a calibration standard to correct the signals of other elements.

#### **ICP:**

Inductively Coupled Plasma (ICP) is a technique used for the detection of chemical elements, primarily in the context of trace metal analysis. It is known for its high sensitivity and precision in quantitative analysis.

For ICP measurements, the instrument parameters were set as follows:

RF Power: 1,150W

Plasma Flow: 0.5 L min $^{-1}$

Auxiliary Flow: 0.5 L min $^{-1}$

Nebulizer Flow: 12.5 L min $^{-1}$

Sample Uptake Delay: 30 seconds

**EPR:**

Electron Paramagnetic Resonance (EPR), also known as Electron Spin Resonance (ESR), is a spectroscopic technique used to observe species with unpaired electrons, such as free radicals or transition metal ions. It provides detailed information about the electronic structure and dynamics of these species.

The EPR measurements were conducted using the following instrument and parameters:

Instrument: Bruker EMXplus-6/1, made in Germany. Test Procedure: Solid samples were ultrasonically dispersed in an appropriate solvent to prepare a  $1 \text{ mg mL}^{-1}$  solution. An equal volume of this dispersion was mixed with a trapping agent. A capillary tube was then used to draw an adequate amount of the mixture, which was placed into a quartz tube and inserted into the sample cavity of the instrument. After tuning the instrument and setting the parameters, the spectrum was scanned and saved for analysis.

## **Supplementary Note Discussion SND 5-2**

### **Discussion on each part of the characterization**

To enhance the comprehensiveness of our study, we used RuO<sub>2</sub>-400/500 as a baseline for comparison. Additionally, we examined the pre-acid wash states of all six samples, including samples A to D, to establish additional control samples.

#### **SEM**

SEM was employed as the first method to investigate the morphology of the as-synthesized samples at various magnifications for an initial assessment. The results for the 12 samples, as depicted in **Figs. SN 5-1-SN 5-12**, reveal that the synthesized samples predominantly consist of interconnected nanoparticles. The control samples, RuO<sub>2</sub>-400/500, and their states prior to acid washing, displayed no significant presence of large particles under 100k magnification (as shown in **Figs. SN 5-9~SN 5-12**). However, only sample C exhibited a morphology closely resembling this characteristic. Under the same magnification, sample C appeared to be composed of smaller nanoparticles, like the control samples. In contrast, the other samples, particularly samples A and D (refer to **Fig. SN 5-1d** and **Fig. SN 5-4d**), exhibited noticeable large aggregate particles, potentially reaching diameters at the micron level. This observation, in conjunction with the discussion in the main text, suggests that the primary initial phase in samples A, B, and D may not be predominantly RuO<sub>2</sub>. Instead, based on XRD analysis, these samples are likely to also include Ca oxides, SrRuO<sub>3</sub>, CaRuO<sub>3</sub> and other possible oxides. The perovskite structures in these samples appear to be more conducive to the annealing process, facilitating the growth of larger crystals.

Combined with observation on high-resolution TEM, our observations in general concluded that the obtained pre-acid wash samples comprised amorphous oxide nanoparticles with considerable porosity, and the metal elements used in the precursor were uniformly distributed. Post acid wash, the morphology pattern remained almost unchanged. However, in comparison to RuO<sub>2</sub>-400/500, sample A, B, and D exhibited larger, aggregated particles, while sample C kept a smaller particle size akin to RuO<sub>2</sub>-400/500.

#### **TEM**

Consistent with the findings presented in the main text, we extended our investigation to all other samples. Initially, we could find that all samples seem to be interconnected single crystal RuO<sub>2</sub> particles. To confirm lattice changes, we examined high-resolution TEM images of the same areas for RuO<sub>2</sub> nanocrystals. For a fair comparison, we aligned the crystal axes (*u v w*) = (1 -1 1) across all samples. We selected specific areas of interest to perform FFT analysis on the diffraction patterns. Additionally, we manually selected regions within these areas to calculate an average interplanar spacing, based on the average of five layers. This approach facilitated a comprehensive comparison, as summarized in **Fig. SN 5-13 (fig. S29 in major Supplementary Materials document)**. Our primary focus was on the RuO<sub>2</sub> (1 1 0) and (1 0 1) facets, which, as indicated by XRD spectra, are the main low-index facets and thus representative of the changes occurring post-doping. For the (1 1 0) facet, except for one outlier in sample A measured by FFT, all other samples A~D exhibited larger interplanar spacings than the control sample RuO<sub>2</sub>-400/500, both in TEM observations and FFT analysis. Moreover, compared to the literature-reported values for perfect crystal RuO<sub>2</sub> (1 1 0), sample C also showed a larger spacing. Similarly, for

the (1 0 1) facet, the results support the notion that doping in samples A, B, C, and D enlarges the interplanar spacing.

Regarding the EDX analysis performed in dark-field conditions, as shown in **Figs. SN 5-14-SN 5-22**, it is evident, as stated in the main text, that there is no significant aggregation of doping elements. They are uniformly distributed with Ru, indicating their possible incorporation into the lattices or at least not forming single metal oxides.

### XRD

XRD analyses further substantiate our earlier assertion that doping has altered the lattice parameters, typically evidenced by XRD peaks shifting to lower angles. The XRD results, summarized in **Fig. SN 5-23-SN 5-31**, clearly demonstrate that for the RuO<sub>2</sub>-400/500 samples and their states before acid washing, the RuO<sub>2</sub> (1 1 0) and (1 0 1) peaks align well with standard powder diffraction files.

Due to the complexity of the precursors in the quaternary oxide system, the XRD spectra revealed not only the main phases of Ca oxides, CaRuO<sub>3</sub>, and RuO<sub>2</sub>, but also a variety of impurities, indicating the co-existence of multiple oxide by-products in the A~D-“Pre” samples before acid wash. Notably, A/B/D-“Pre” samples also revealed the presence of SrRuO<sub>3</sub>. A, B, and D continued to exhibit traces of CaRuO<sub>3</sub> and SrRuO<sub>3</sub> while for C, such secondary phases are proven completely removed. Such perovskites are known by previous consensus in the field to dissolve cations causing irreversible collapse of polynmetallic oxide structures<sup>1, 2, 3</sup>, possibly effect the stability of RuO<sub>2</sub> main body. This might explain the inferior stability behavior of A, B, and D compared with C.

Moreover, for sample C, the RuO<sub>2</sub> (1 1 0) and (1 0 1) peaks have shifted towards lower angles as anticipated. Furthermore, for the C-Pre sample, the CaRuO<sub>3</sub> (1 1 2) peak, also shifted towards a lower angle. This pattern is consistent across samples A/B/D, and their states prior to acid washing. This suggests that the dopants may have influenced the perovskite structures before acid washing, and this influence persisted post-washing, continuing to affect the RuO<sub>2</sub> lattice. At this point, we can determine that C is an oxide doped with multiple metals, while A, B, and D, although it can be seen from XRD that there are no obvious presence of other single metal oxides or unstable oxides in other acids, they are still CaRuO<sub>3</sub> and SrRuO<sub>3</sub> phases exist in small amounts.

### Quantitative analysis (ICP, EPR, XPS and other element content analysis)

ICP analysis serves as a crucial tool for determining the elemental composition of our samples. While ICP offers a high accuracy in assessing the entire bulk material, XPS provides a semi-quantitative analysis of the estimated atomic percentages of each element on the surface, offering an additional perspective for a more comprehensive understanding. These results are summarized in **Fig. SN 5-32 (fig. S30 in major Supplementary Materials document)**. The variation trends in element contents before and after acid washing, as observed in both ICP and XPS analyses, exhibit a consistent pattern, reflecting the uniformity between the bulk and surface compositions. Specifically, for samples A, B, and D (**Fig. SN 5-32 a, b, d**), we observed an increase in Ru content, a decrease in Ca content, an increase in Sr content, and a decrease in Nd content post-acid wash. For sample C (**Fig. SN 5-32c**), the trends include an increase in Ru content, a decrease in Mn and Ca contents, and a reduction in Pr content post-acid wash. These trends, combined with the data in **Fig. SN 5-32e**, provide insights into the chemical changes occurring during the process. For samples A, B, and D, the acid wash appears to remove unstable oxide species especially calcium oxide, which are predominantly observed in the XRD spectra. Nd

content also decreases, leaving only a trace amount, possibly indicative of the doping level in the RuO<sub>2</sub> lattice. However, Sr content, unlike Ca, does not diminish but slightly increases, similar to Ru. However, considering the stoichiometric ratio, Ru's signal are predominantly higher than other metal elements based on quantification results. We could apparently conclude the fact that perovskite phases are not likely to be exposed on the surface like RuO<sub>2</sub> that we could observe in the surface quantification of element signals through EDX via SEM and TEM (**Fig. SN 5-34**). Hence, we suggest that for A, B, and D, the Sr and Ca rich perovskite phase are covered by RuO<sub>2</sub> on the surface. Combining with the fact that CaRuO<sub>3</sub> and SrRuO<sub>3</sub> are dominant in A,B,D-Pre, and also the previous report of how these Ru containing perovskite would evolve to Ru oxides in acidic electrolyte, we could clear conclude that Sr and Ca were dissolved causing irreversible collapse of polymetallic oxide structures, remaining only Ru oxide clusters on the surface with Sr and Ca enriched secondary perovskite phase in the inner body<sup>1, 2, 3, 4, 5</sup>.

In the case of sample C, the removal of Ca species, primarily existing as calcium oxide before acid washing, is evident. Additionally, the Pr content, like Nd, decreases to trace levels, as both are rare-earth elements selected by the ML committee after five iterations. And no remain of CaRuO<sub>3</sub> and SrRuO<sub>3</sub> like A/B/D could be observed like indicated in **Fig. 5E**. Notably, Mn content also shows a significant decrease, both in ICP and XPS surface analyses. Combined with the XRD spectra of sample C, this suggests that Mn oxides are removed during acid washing, leaving primarily doped RuO<sub>2</sub>. The EPR results in **Fig. SN 5-33** (**Fig. S31** in major **Supplementary Materials** document) further support this conclusion. Among the 12 samples, C-Pre exhibits the highest levels of magnetism-related metrics: magnetic susceptibility, total spins, and spins per cubic millimeter, consistent with the presence of strong magnetism in C-Pre due to Mn oxide. During TEM analysis, C-Pre was the only sample to exhibit noticeable magnetism, as evidenced by attraction to a magnet. Post-acid washing, the EPR results show a significant reduction in the magnetism of the final product, sample C, possibly indicating the absence of strongly magnetic Mn oxide, with the remaining Mn successfully doped into the RuO<sub>2</sub> lattice.

**Figs. SN 5-34-SN 5-35** summarize the SEM and TEM EDX mapping quantitative results for elemental distribution. They still reveal consistent trends in elemental variations before and after acid washing, aligning with the ICP and XPS analysis results. This consistency not only reinforces our previous conclusions but also supports the representativeness of the TEM-selected areas for the entire sample. Therefore, we can confidently trust our conclusions, given the high degree of consistency across different characterization results.

In conclusion, Combining TEM, SEM, and ICP quantitative results, it would be suggested that Ru were the main metal element that should be concerned and RuO<sub>2</sub> with metal dopants is the main phase. CaRuO<sub>3</sub> and SrRuO<sub>3</sub> have shown certain existence in the inner body of A/B/D but are significantly inferior on surface signals. Combined with field consensus by previous reports, it could be concluded that the acid wash process has also dissolve their unstable phases and cations on the surface, remaining Ru oxide clusters on the surface like C. Hence, these Sr and Ca enriched perovskite secondary phases are considered to be embedded under the RuO<sub>2</sub> surface and were not removed by acid wash in the synthesis process (although it harm stability). For the most important sample C, the results further indicated that it is doped RuO<sub>2</sub> with no impurities oxides. In general, we can conclude that the surface of A~D could all be considered as Ru oxides doped with different metal elements in the

inner body. And this is the reason why we choose to use the representative RuO<sub>2</sub> (110) as the subject of theoretical study part, for simplicity and uniformity.

### XPS of C

In our study, XPS analysis, as presented in **Fig. SN 5-36** (Ru 3d) and **Fig. SN 5-37** (Ru 3p), serves as the final characterization tool to delve into the effects of metal elements, introduced by the ML committee, on RuO<sub>2</sub>. For samples A, B, and D, a noticeable shift in the Ru 3d spectra is observed. Compared to RuO<sub>2</sub>-400/500, the 5/2 peaks of these samples have distinctly shifted towards lower binding energies, as indicated by the peak fitting results. However, for sample C, as highlighted in the main text, its 5/2 peak exhibits a slight shift towards a higher binding energy. Furthermore, when examining the Ru 3p peaks, statistical analysis of the peak ratios reveals that sample C possesses the highest ratio of Ru in oxidation states greater than +4. According to previous studies, such as those by Hou et al., this observation could be attributed to a redistribution of charge<sup>6</sup>. Consequently, the adsorbed oxygen intermediates are likely enhanced by the high-valence Ru <sup>>4+</sup> atoms, thereby promoting the OER activity.

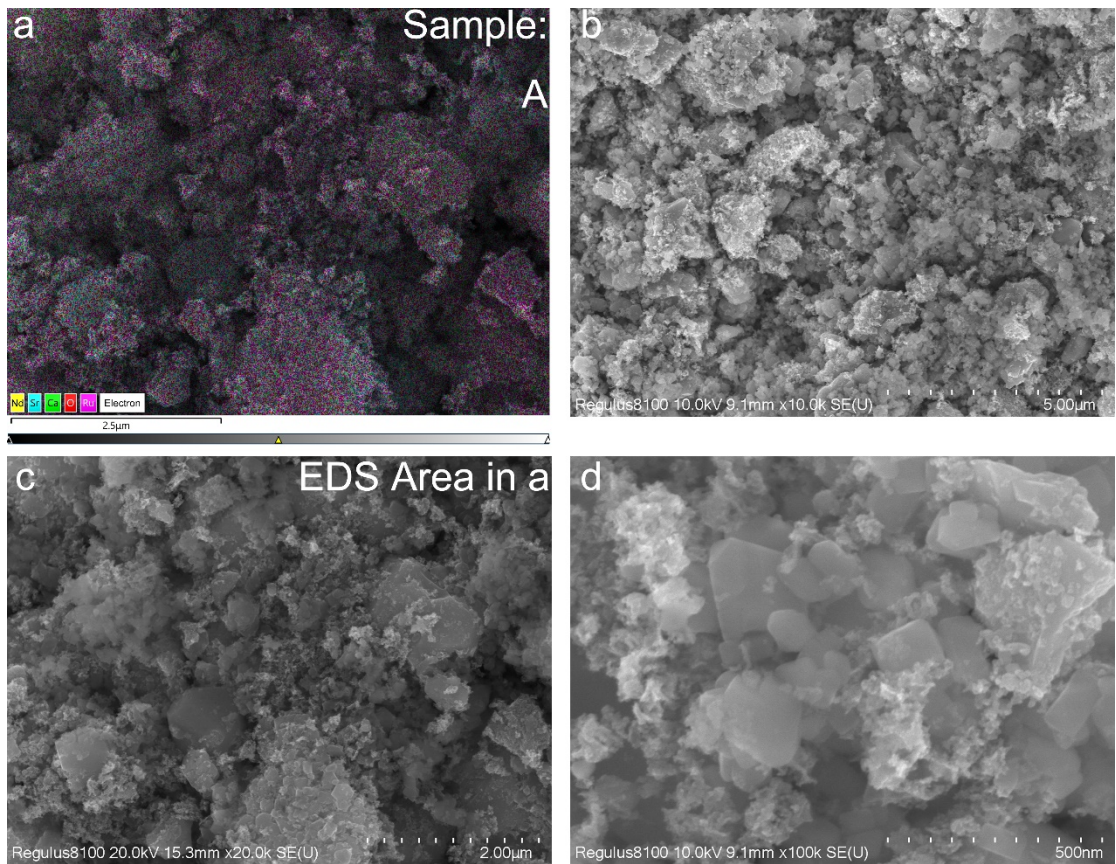


**Fig. SN 5-1** (a) the EDX mapping plots and (b)-(d) SEM images of sample A under different magnifications.

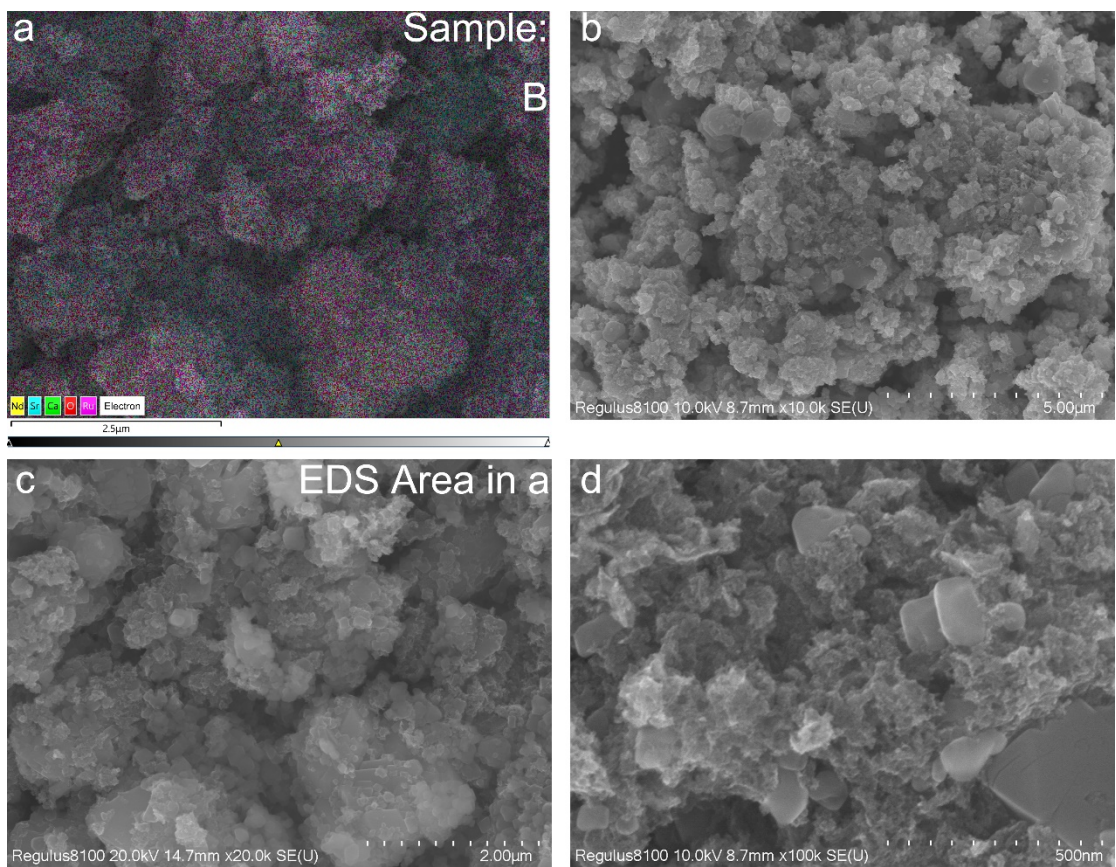


**Fig. SN 5-2** (a) the EDX mapping plots and (b)-(d) SEM images of sample B under different magnifications.

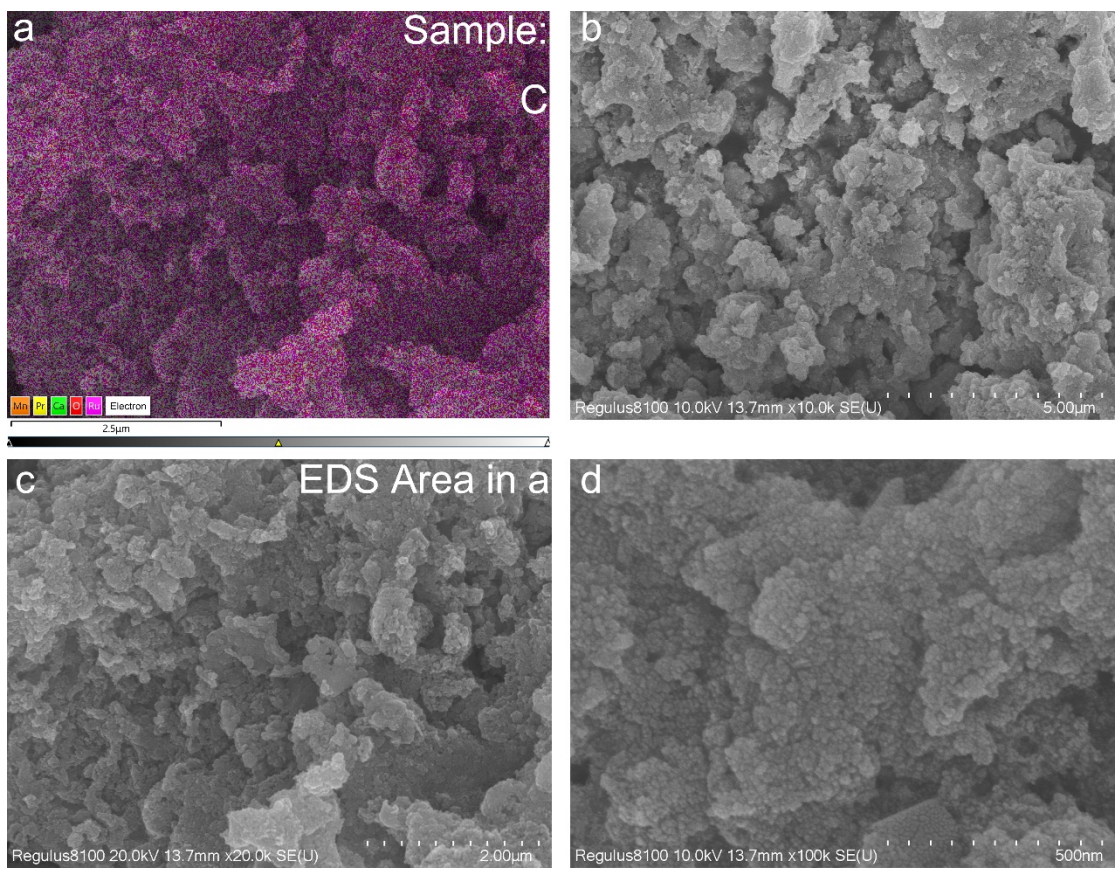


**Fig. SN 5-3** (a) the EDX mapping plots and (b)-(d) SEM images of sample C under different magnifications.

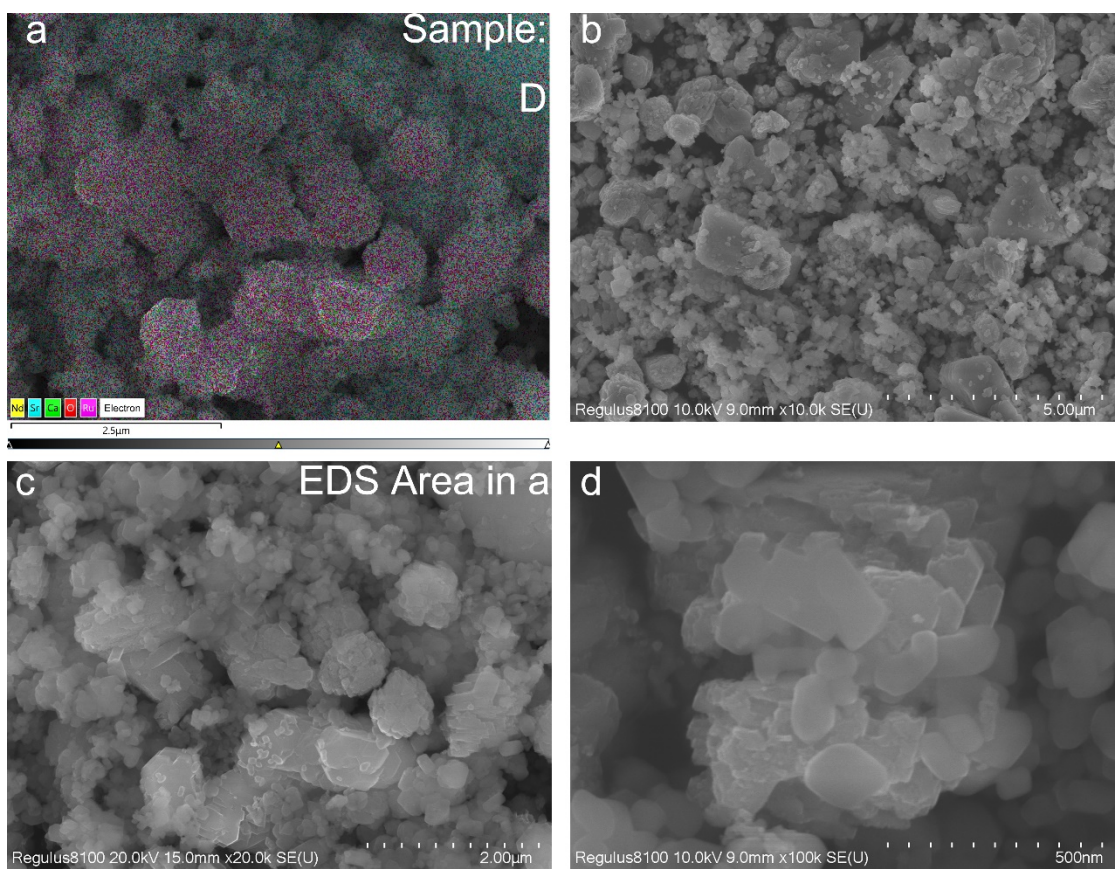


**Fig. SN 5-4** (a) the EDX mapping plots and (b)-(d) SEM images of sample D under different magnifications.

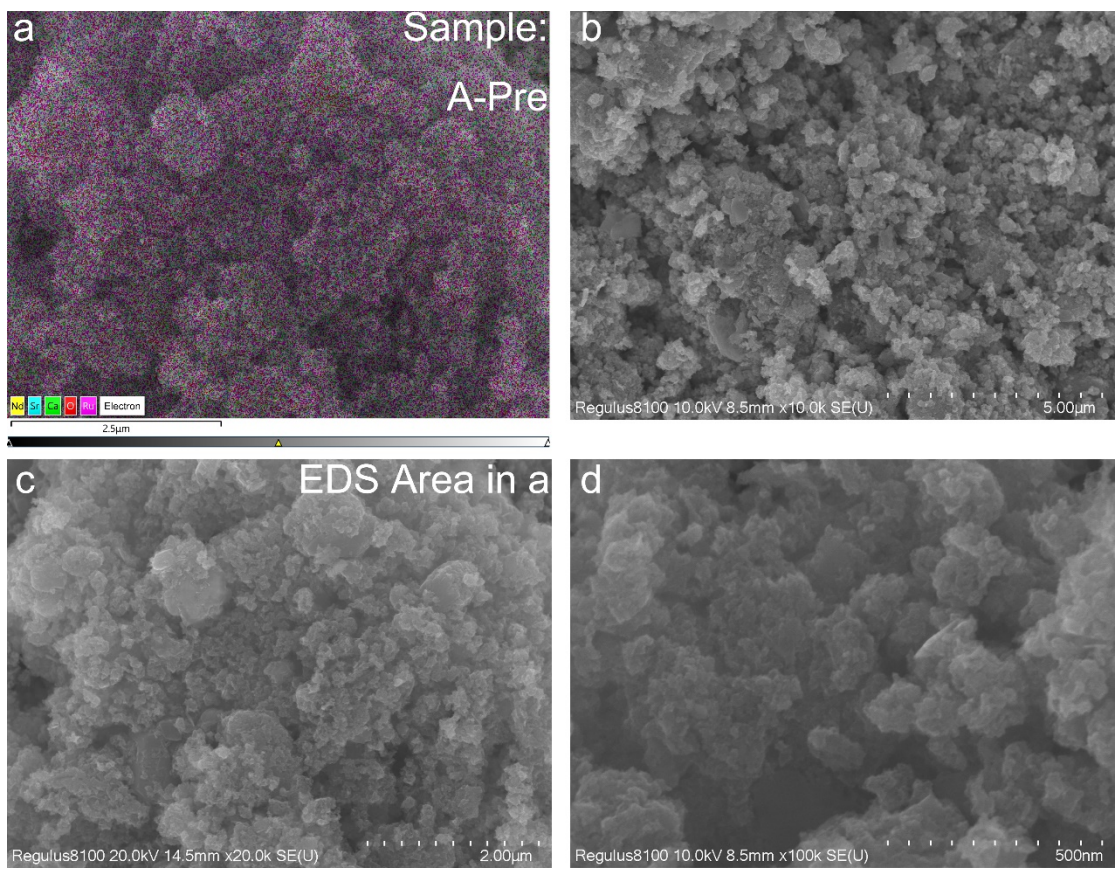


**Fig. SN 5-5** (a) the EDX mapping plots and (b)-(d) SEM images of sample A-Pre under different magnifications.

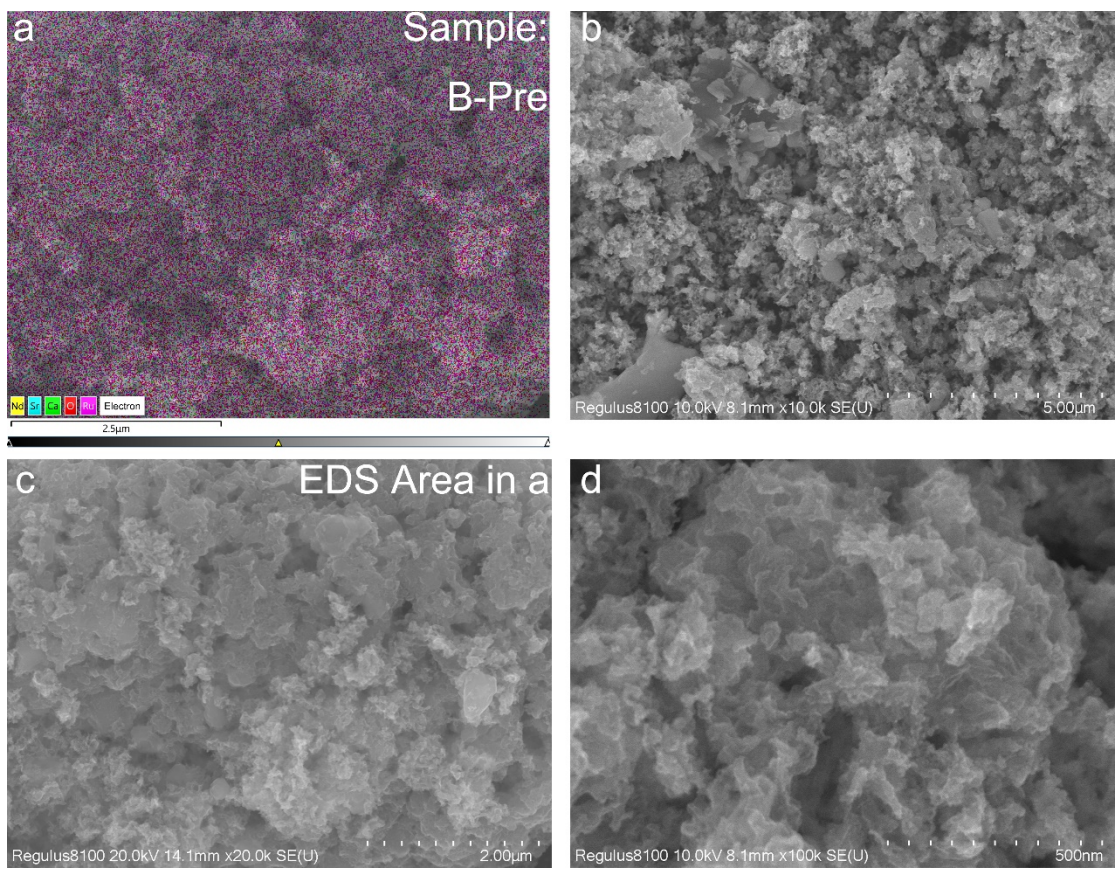


**Fig. SN 5-6** (a) the EDX mapping plots and (b)-(d) SEM images of sample B-Pre under different magnifications.

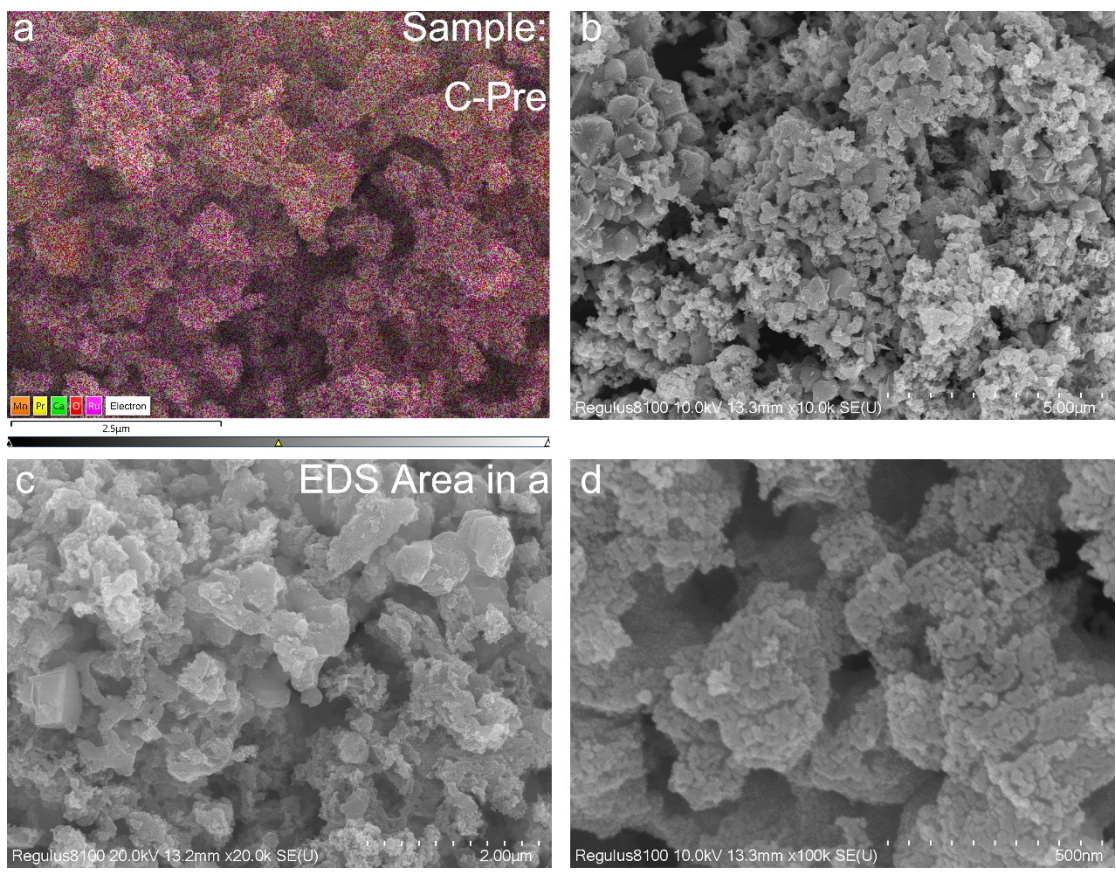


**Fig. SN 5-7** (a) the EDX mapping plots and (b)-(d) SEM images of sample C-Pre under different magnifications.

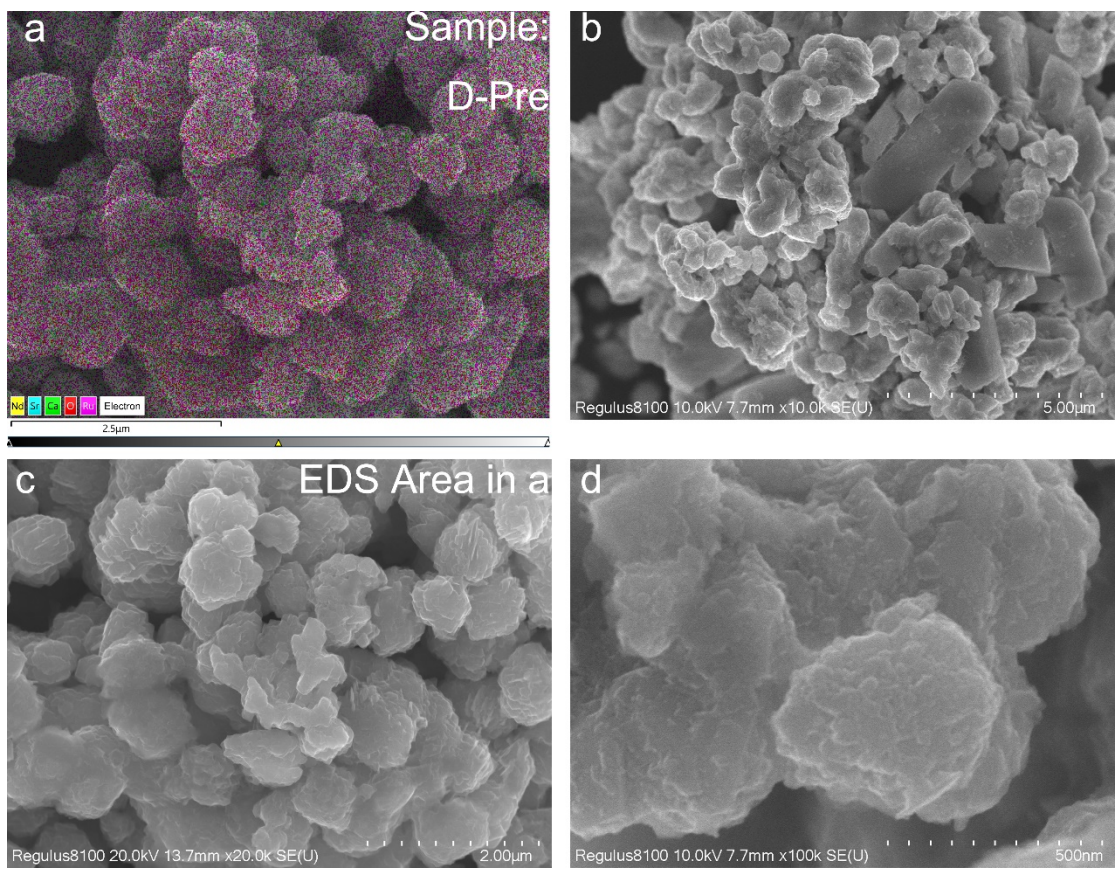


**Fig. SN 5-8** (a) the EDX mapping plots and (b)-(d) SEM images of sample D-Pre under different magnifications.

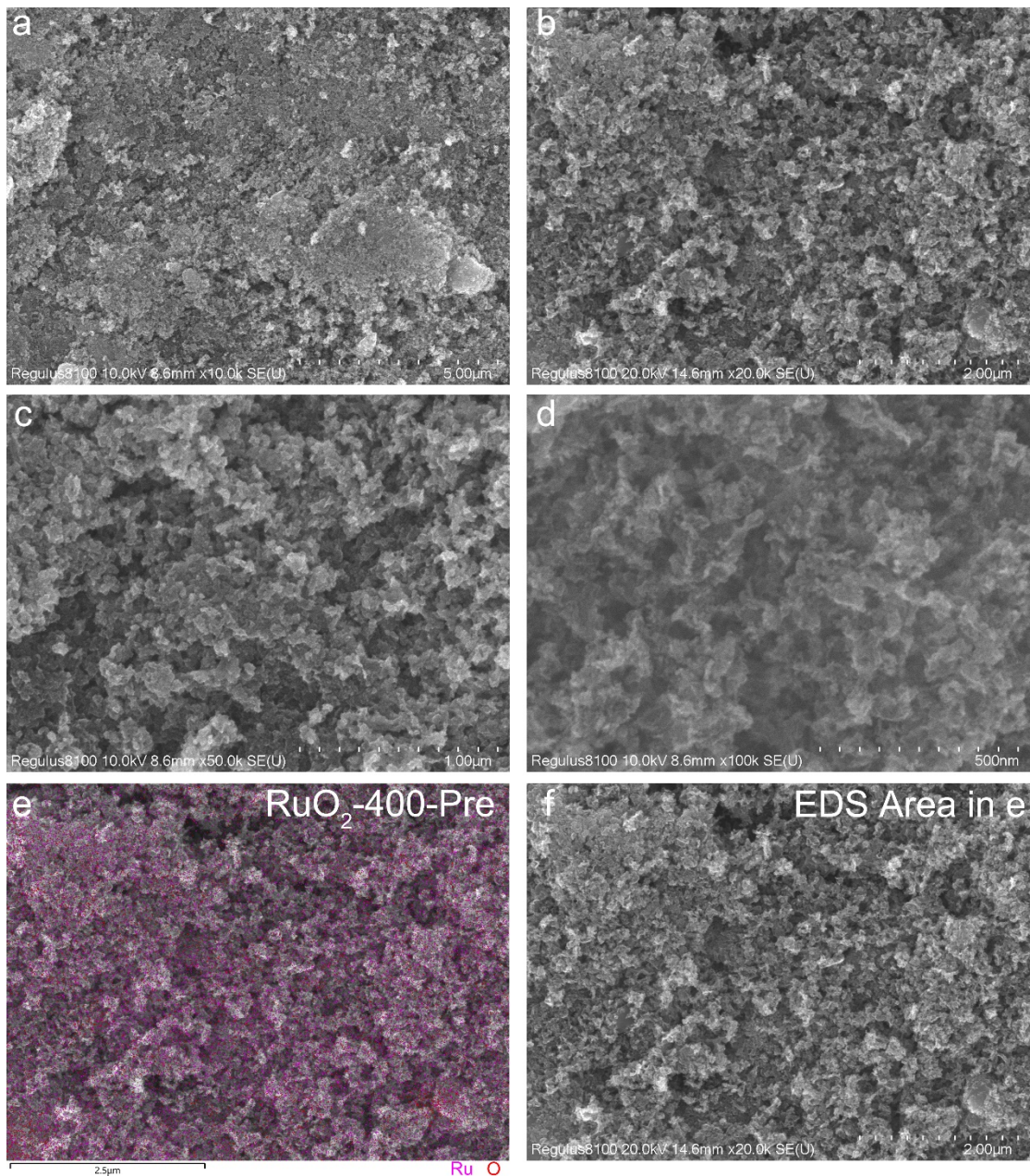


**Fig. SN 5-9** (a)-(d) and (f) SEM images; (e) EDX mapping plot of sample  $\text{RuO}_2\text{-}400\text{-Pre}$  under different magnifications.

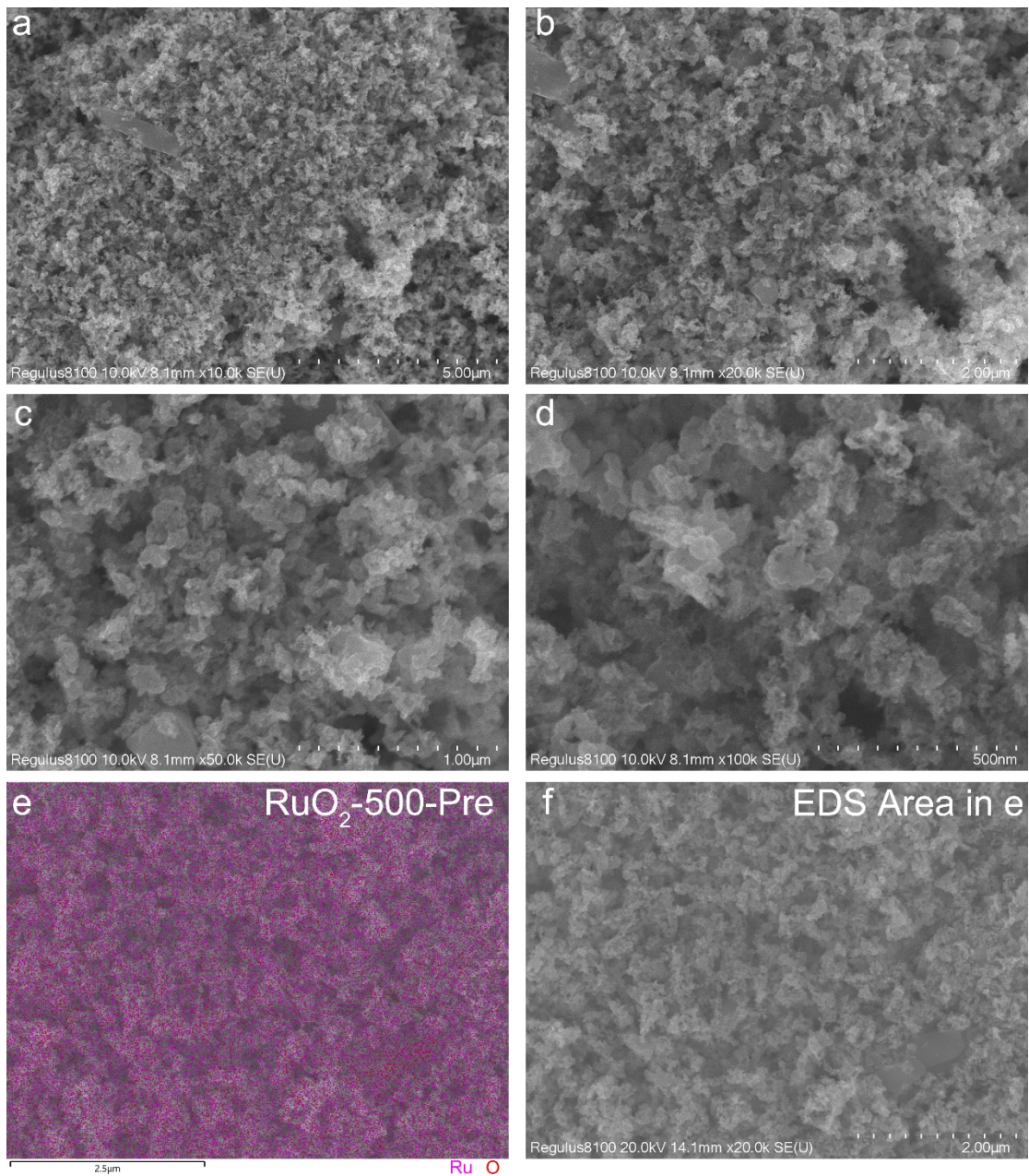


**Fig. SN 5-10** (a)-(d) and (f) SEM images; (e) EDX mapping plot of sample  $\text{RuO}_2\text{-}500\text{-Pre}$  under different magnifications.

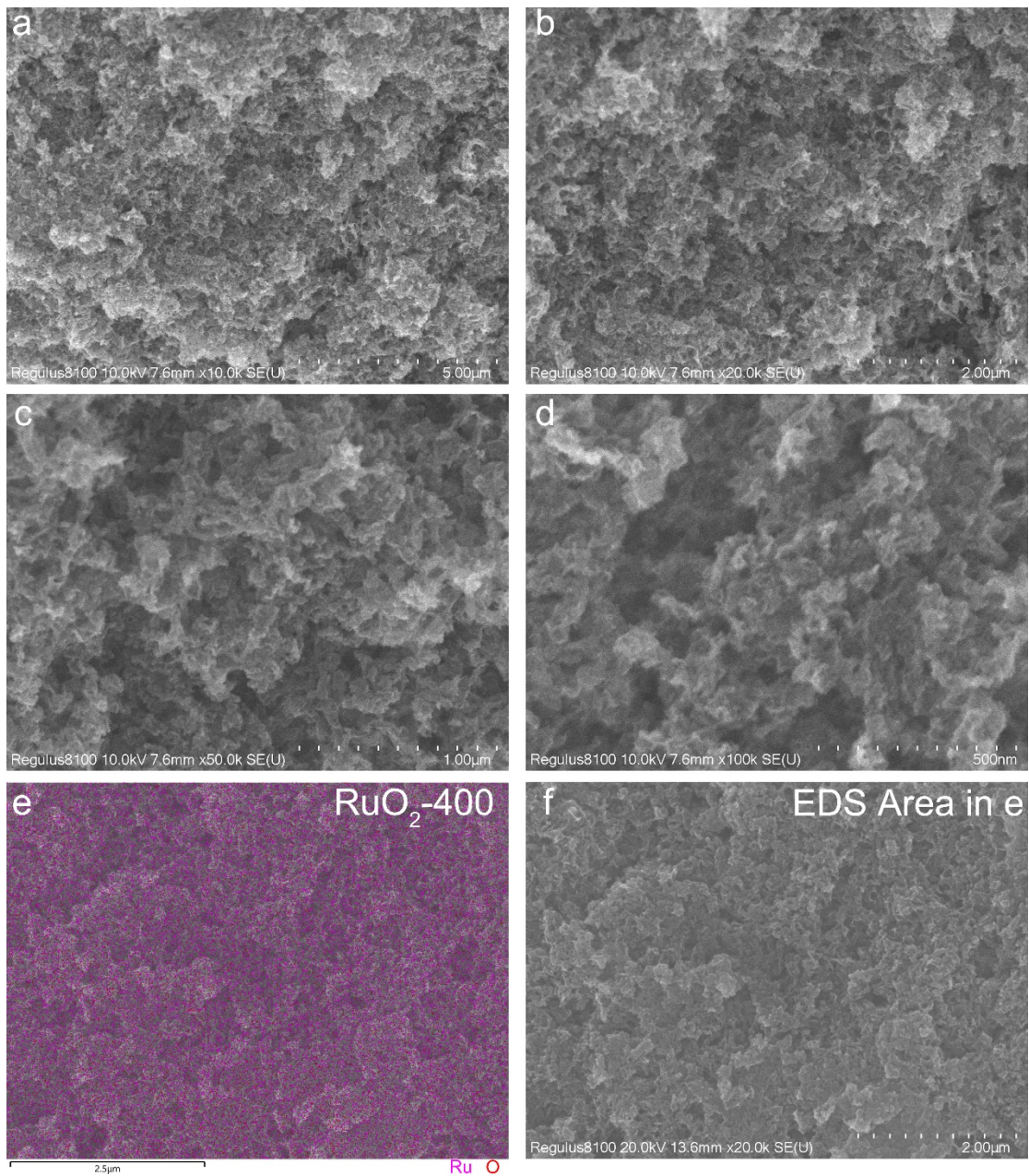


**Fig. SN 5-11** (a)-(d) and (f) SEM images; (e) EDX mapping plot of sample  $\text{RuO}_2\text{-}400$  under different magnifications.

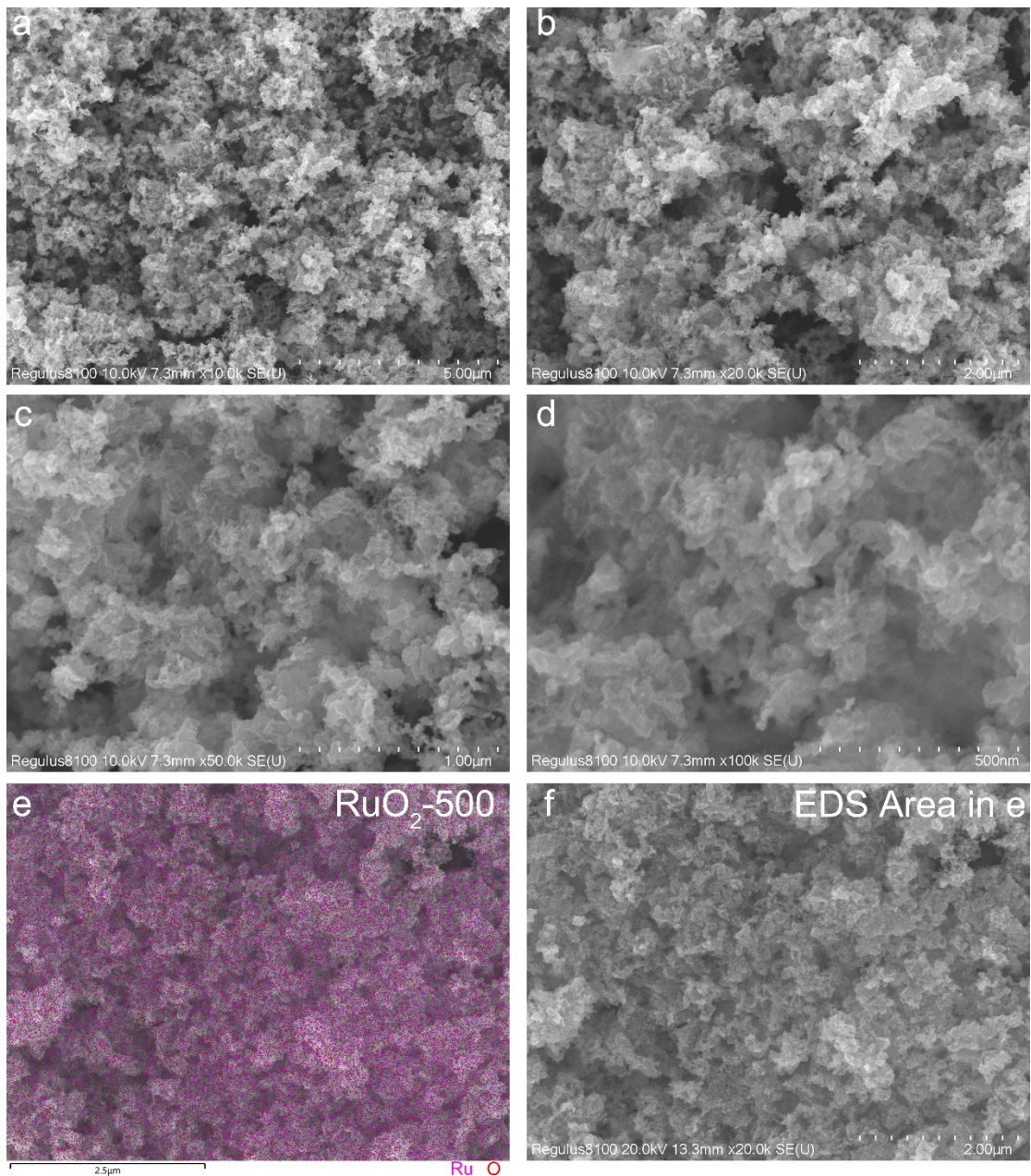


**Fig. SN 5-12** (a)-(d) and (f) SEM images; (e) EDX mapping plot of sample RuO<sub>2</sub>-500 under different magnifications.

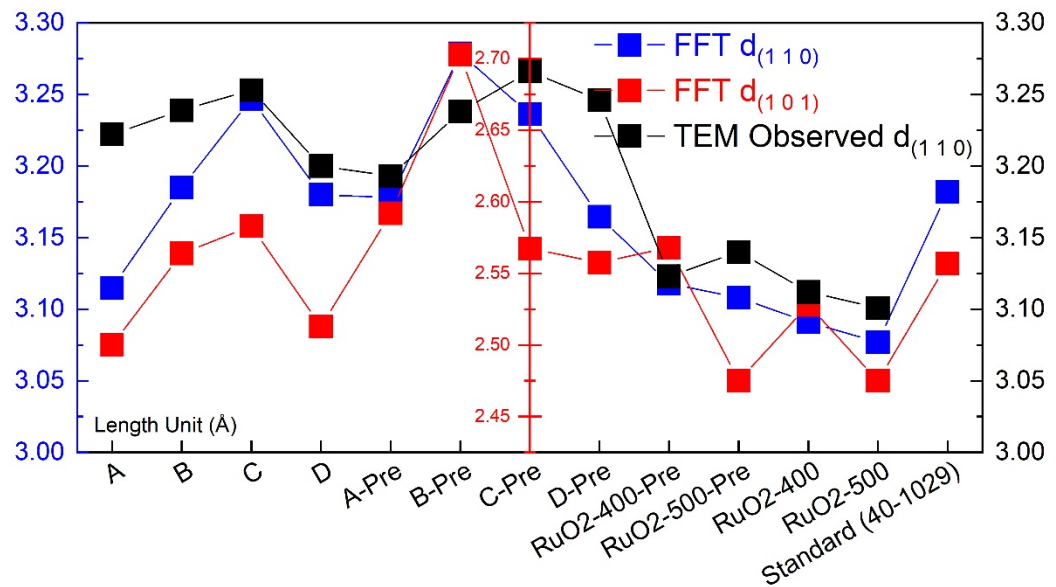


**Fig. SN 5-13** The statistical line graph of the interplanar spacings for the (110) and (101) planes calculated from the inverse space diffraction patterns obtained through selected area FFT transformation, and the average (110) plane spacing directly measured in the selected areas of TEM images for different samples of RuO<sub>2</sub> crystalline particles.

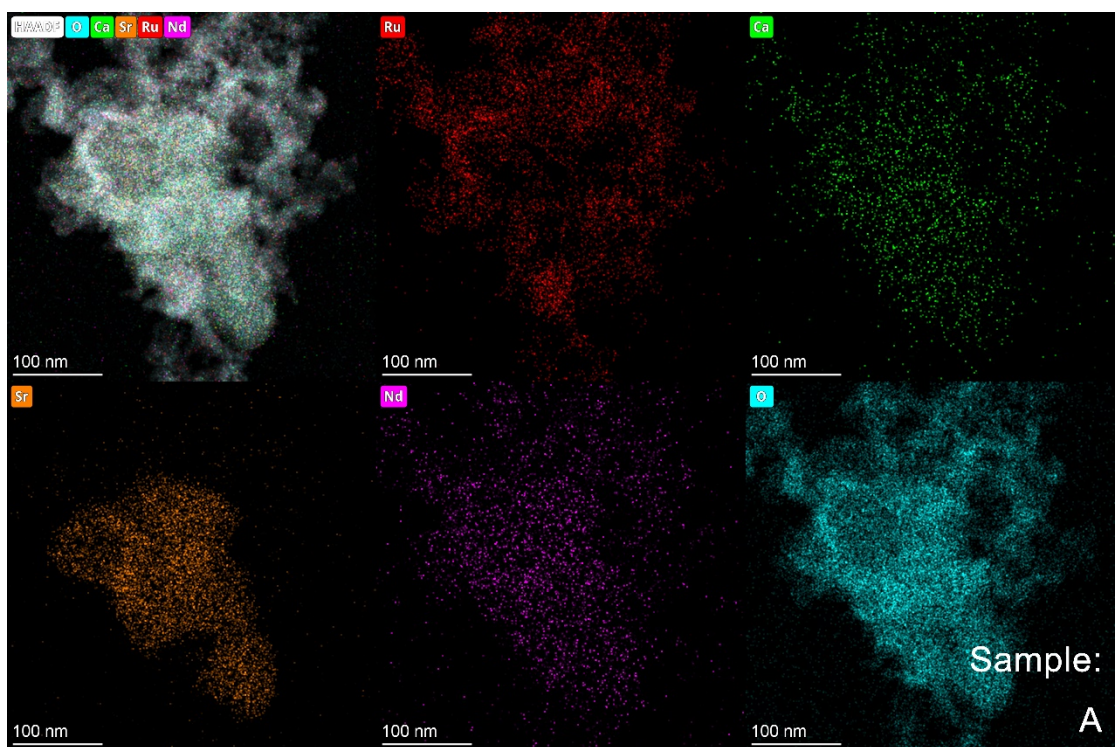


**Fig. SN 5-14** TEM-EDX elemental distribution mapping spectra for sample A.

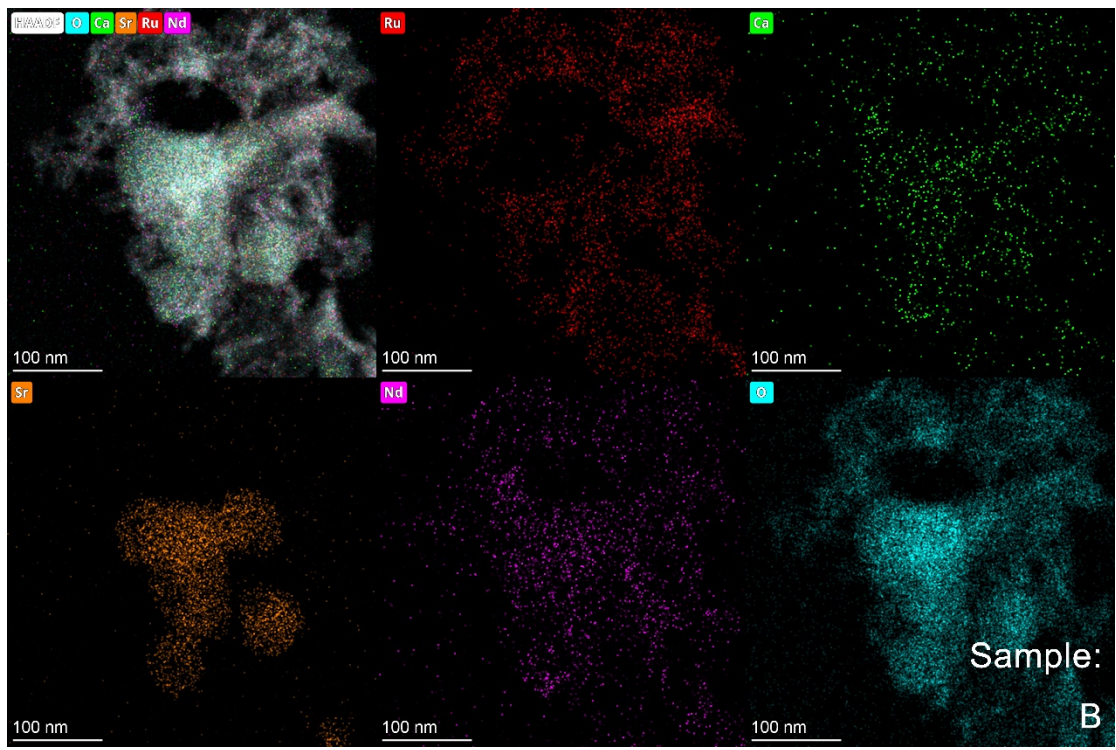


**Fig. SN 5-15** TEM-EDX elemental distribution mapping spectra for sample B.

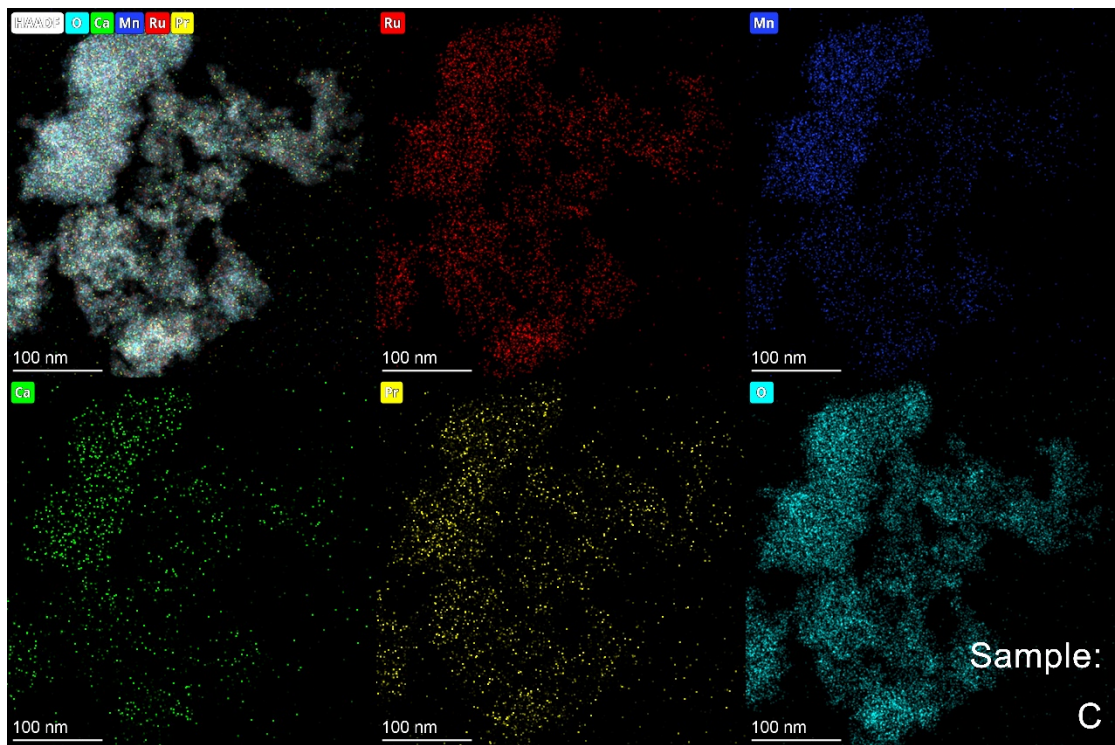


**Fig. SN 5-16** TEM-EDX elemental distribution mapping spectra for sample C.

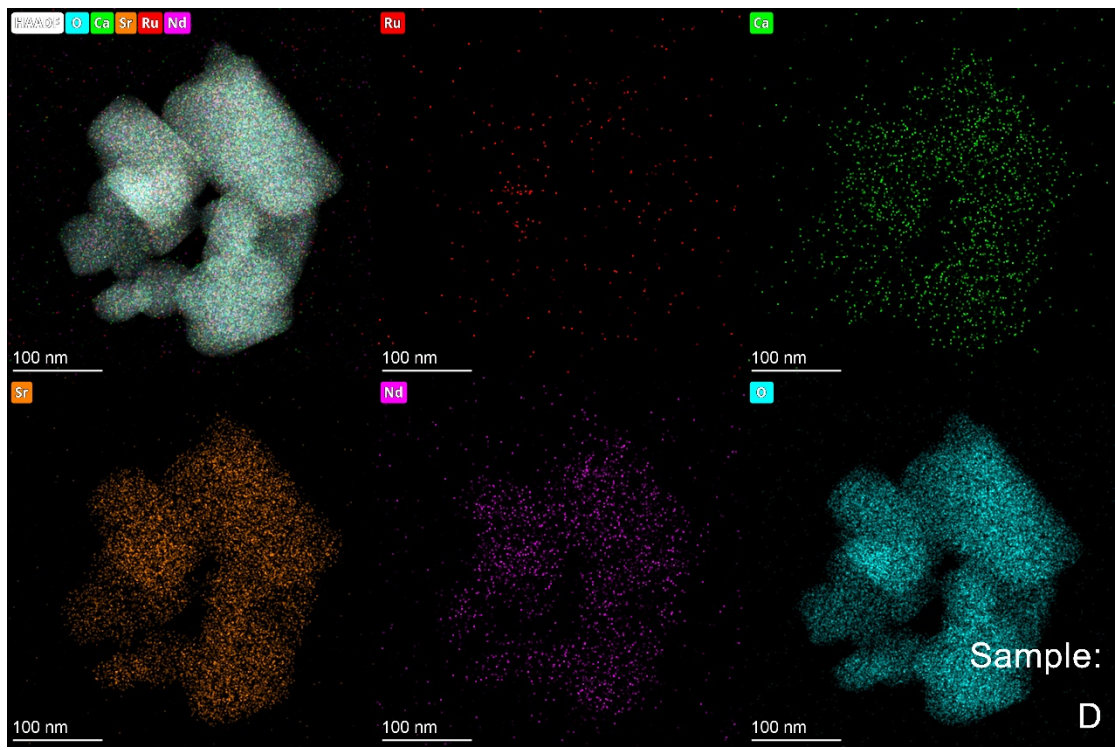


**Fig. SN 5-17** TEM-EDX elemental distribution mapping spectra for sample D.

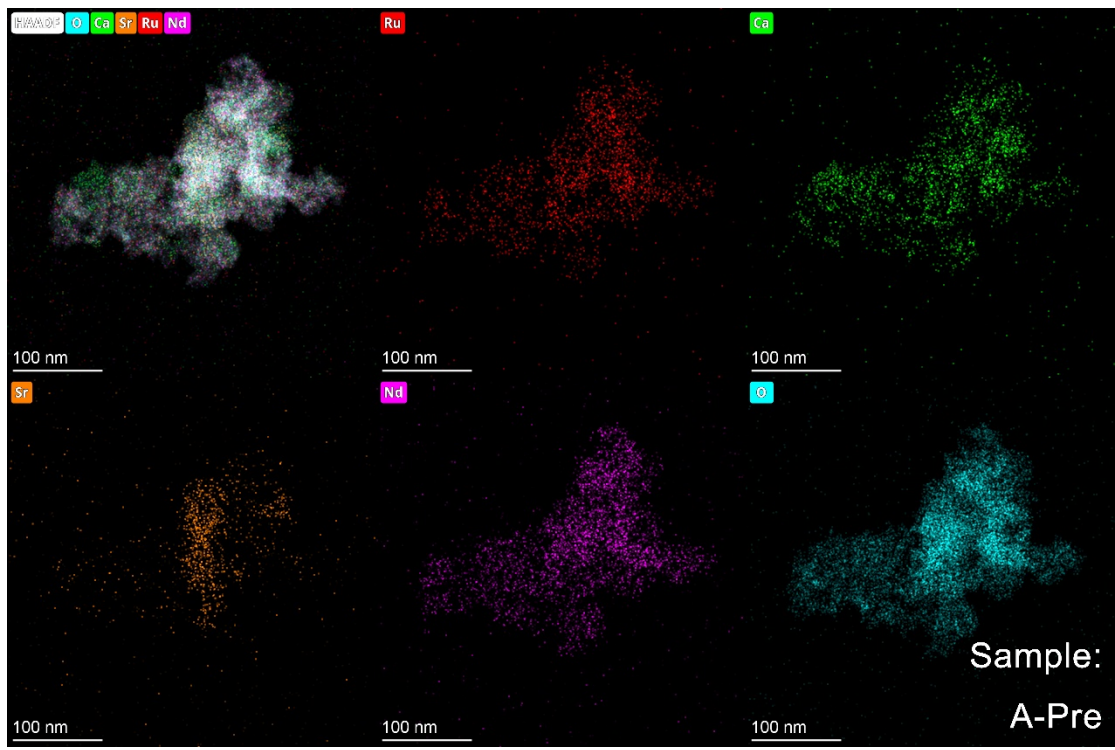


**Fig. SN 5-18** TEM-EDX elemental distribution mapping spectra for sample A-Pre.

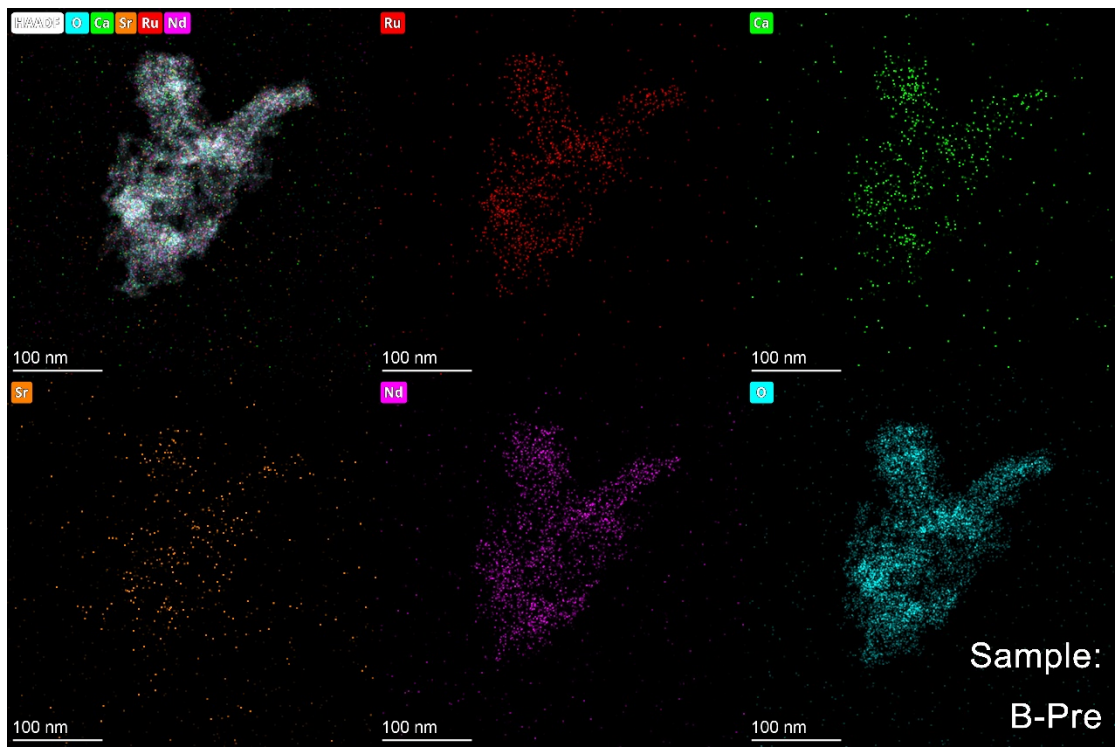


**Fig. SN 5-19** TEM-EDX elemental distribution mapping spectra for sample B-Pre.

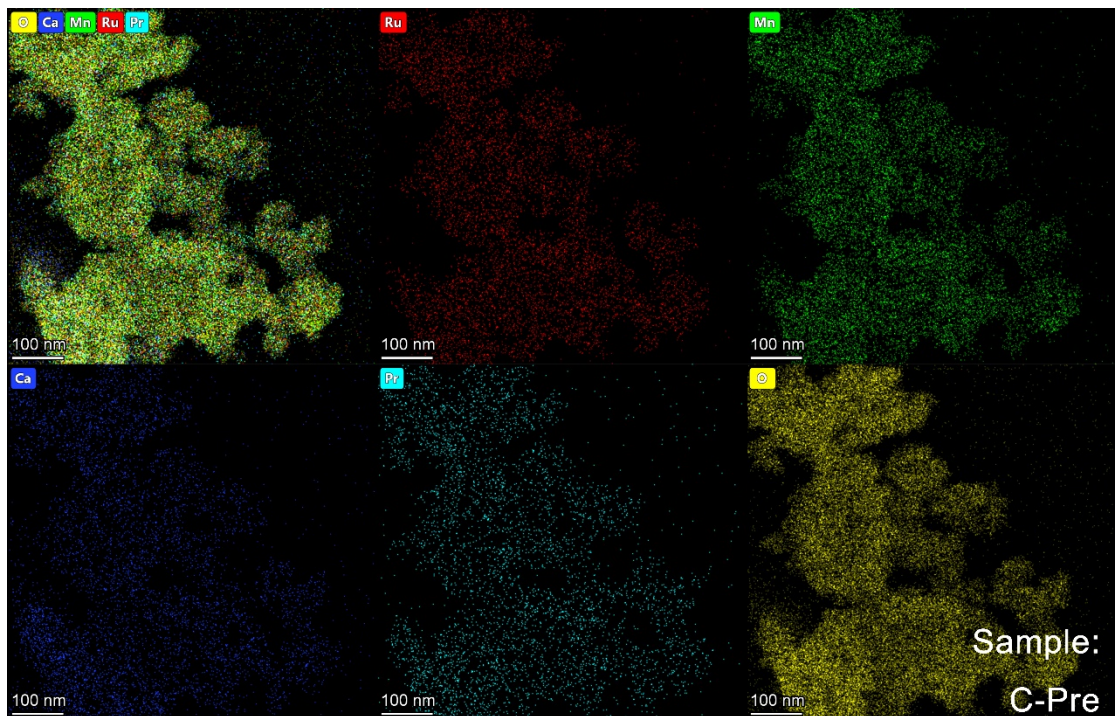


**Fig. SN 5-20** TEM-EDX elemental distribution mapping spectra for sample C-Pre.

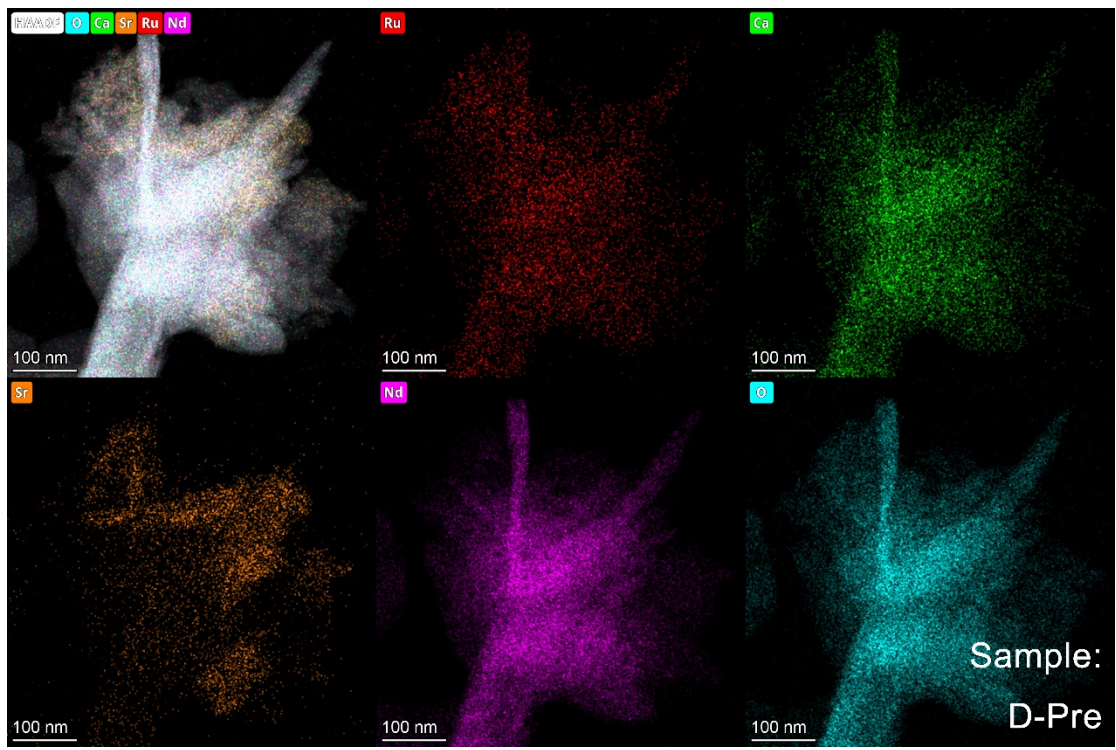


**Fig. SN 5-21** TEM-EDX elemental distribution mapping spectra for sample D-Pre.

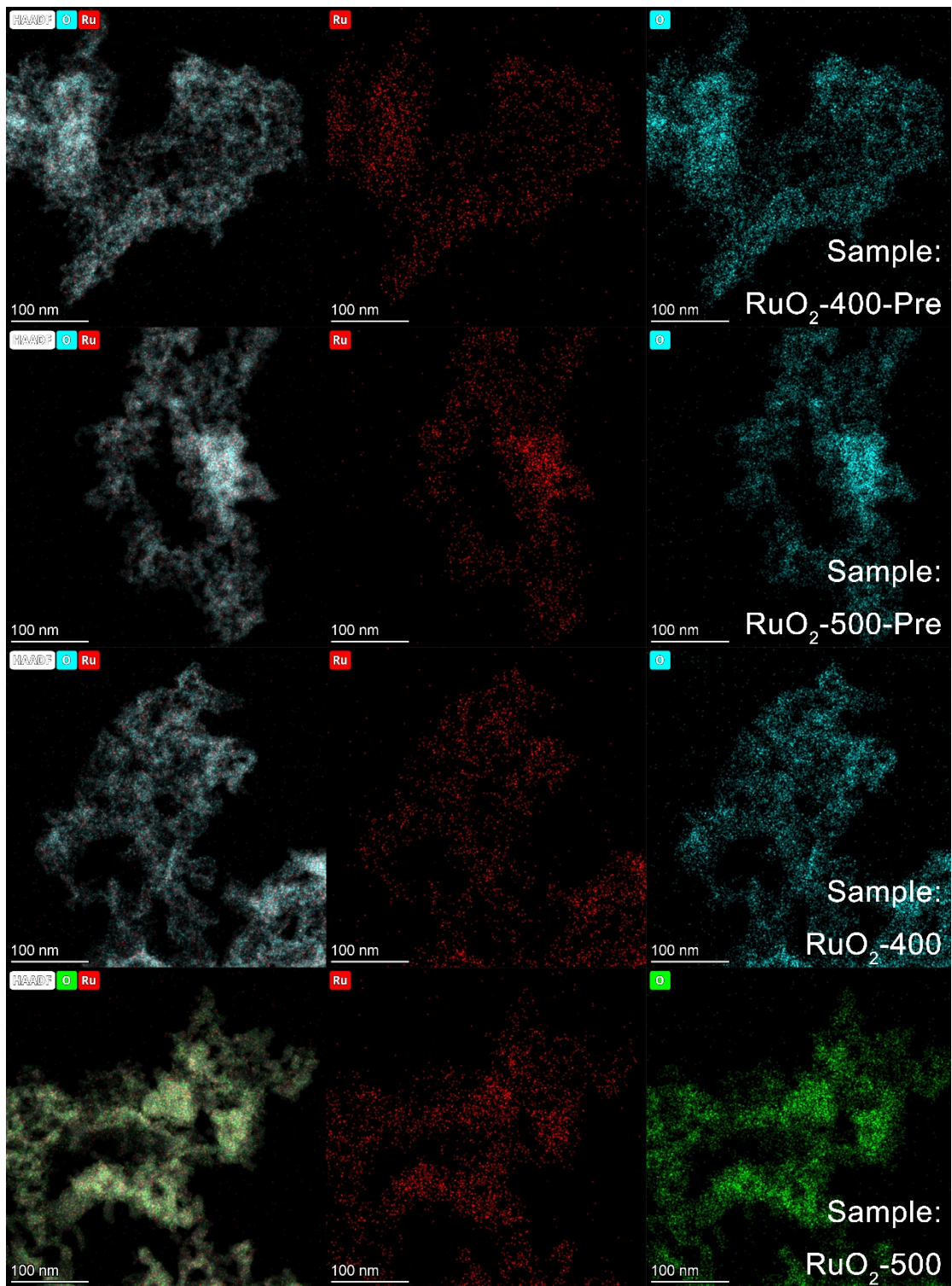


**Fig. SN 5-22** TEM-EDX elemental distribution mapping spectra for pure RuO<sub>2</sub> samples.

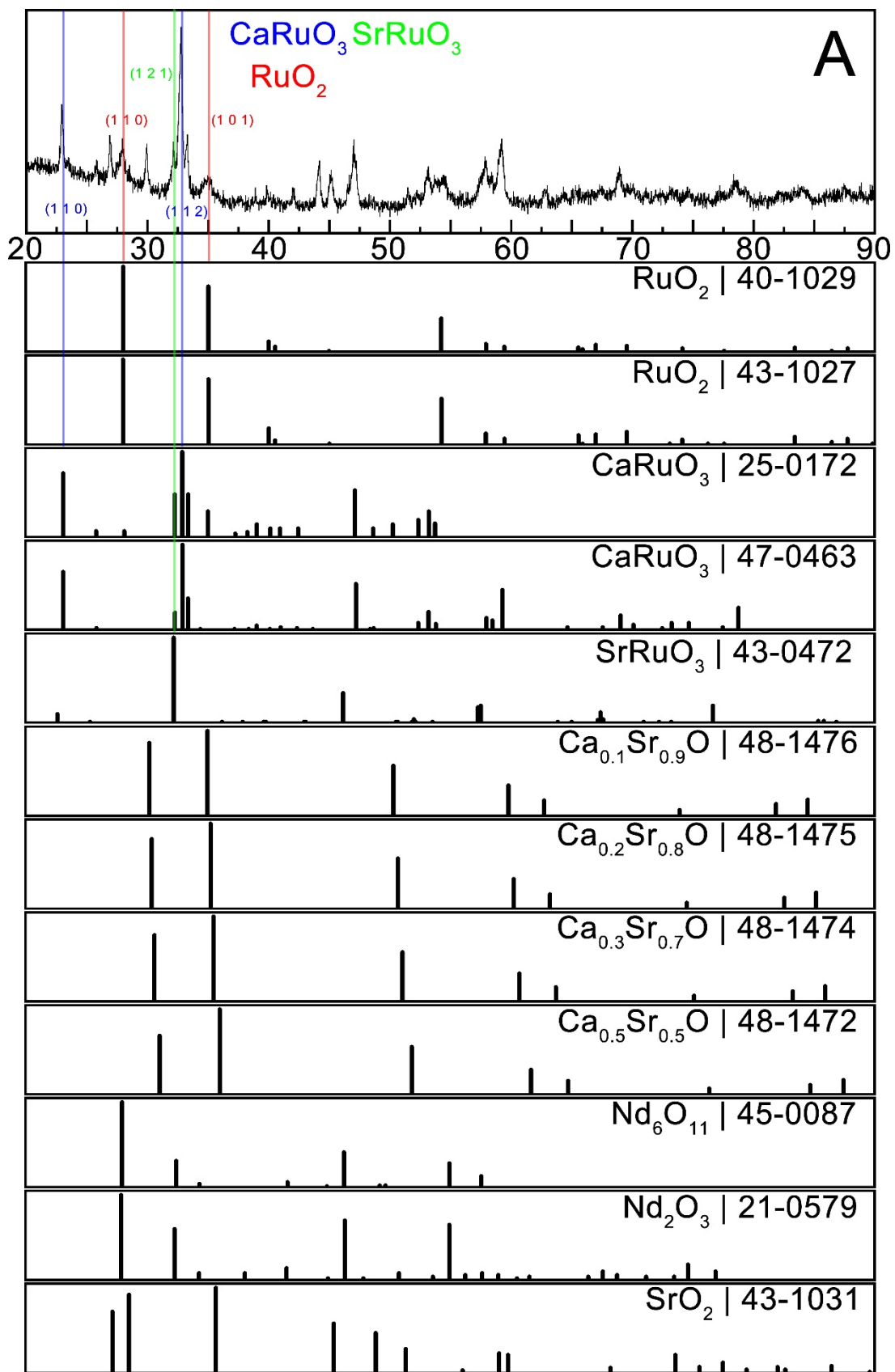


**Fig. SN 5-23** XRD spectra of sample A. Due to complexity and multiple possibilities of existing phases, we only label the dominant peaks and corresponding phases' major facets.

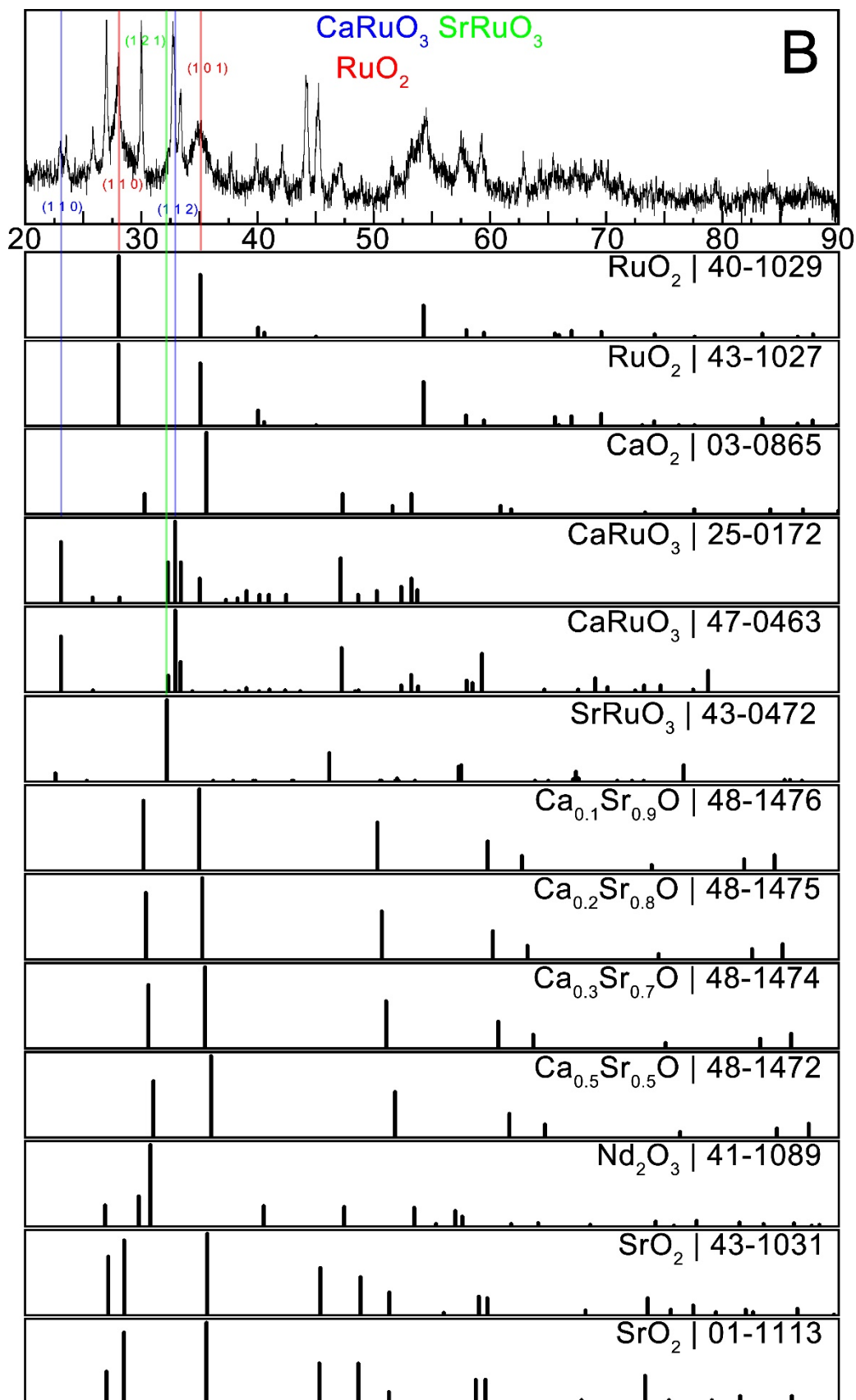


**Fig. SN 5-24** XRD spectra of sample B. Due to complexity and multiple possibilities of existing phases, we only label the dominant peaks and corresponding phases' major facets.

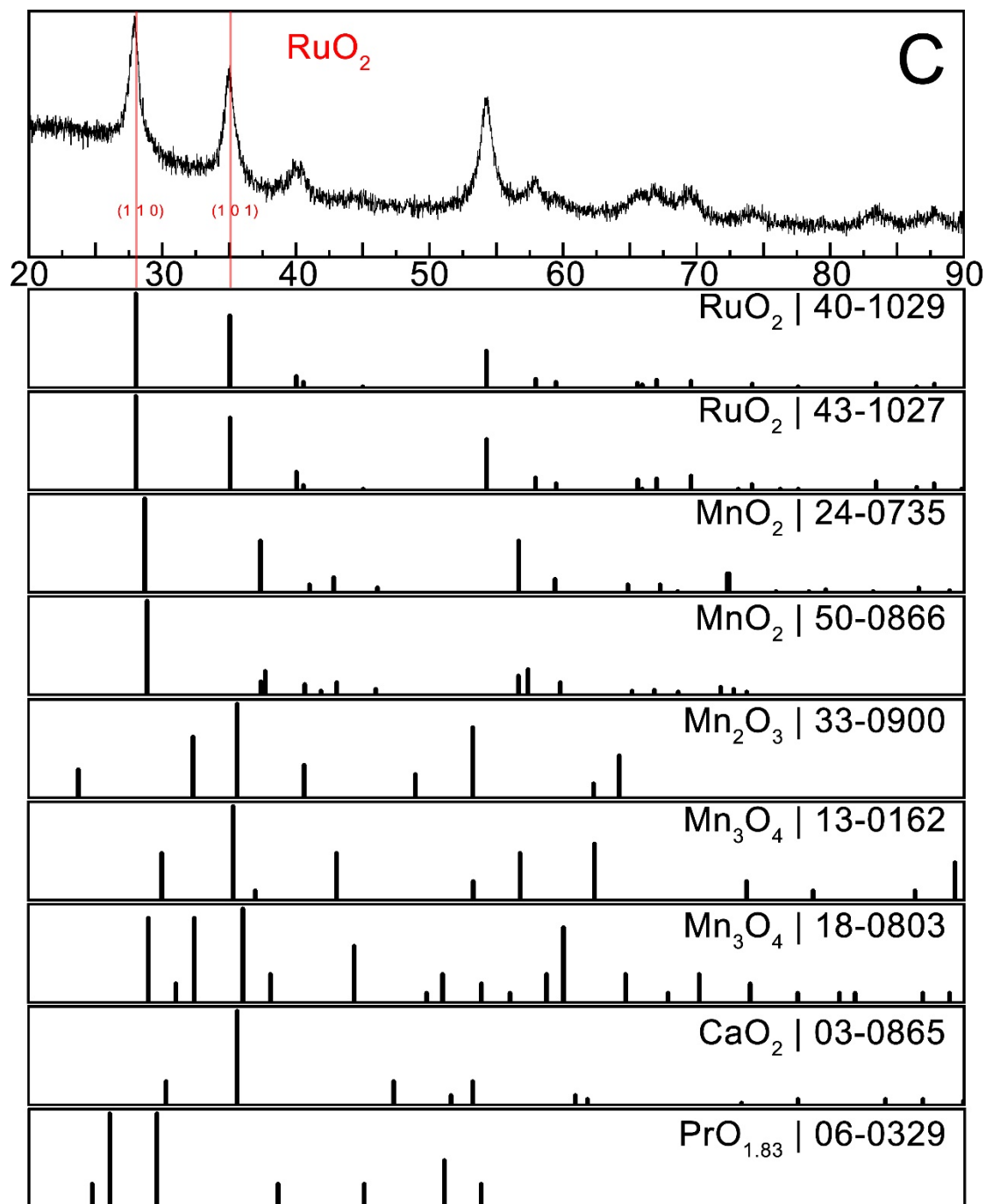


**Fig. SN 5-25** XRD spectra of sample C. Due to complexity and multiple possibilities of existing phases, we only label the dominant peaks and corresponding phases' major facets.

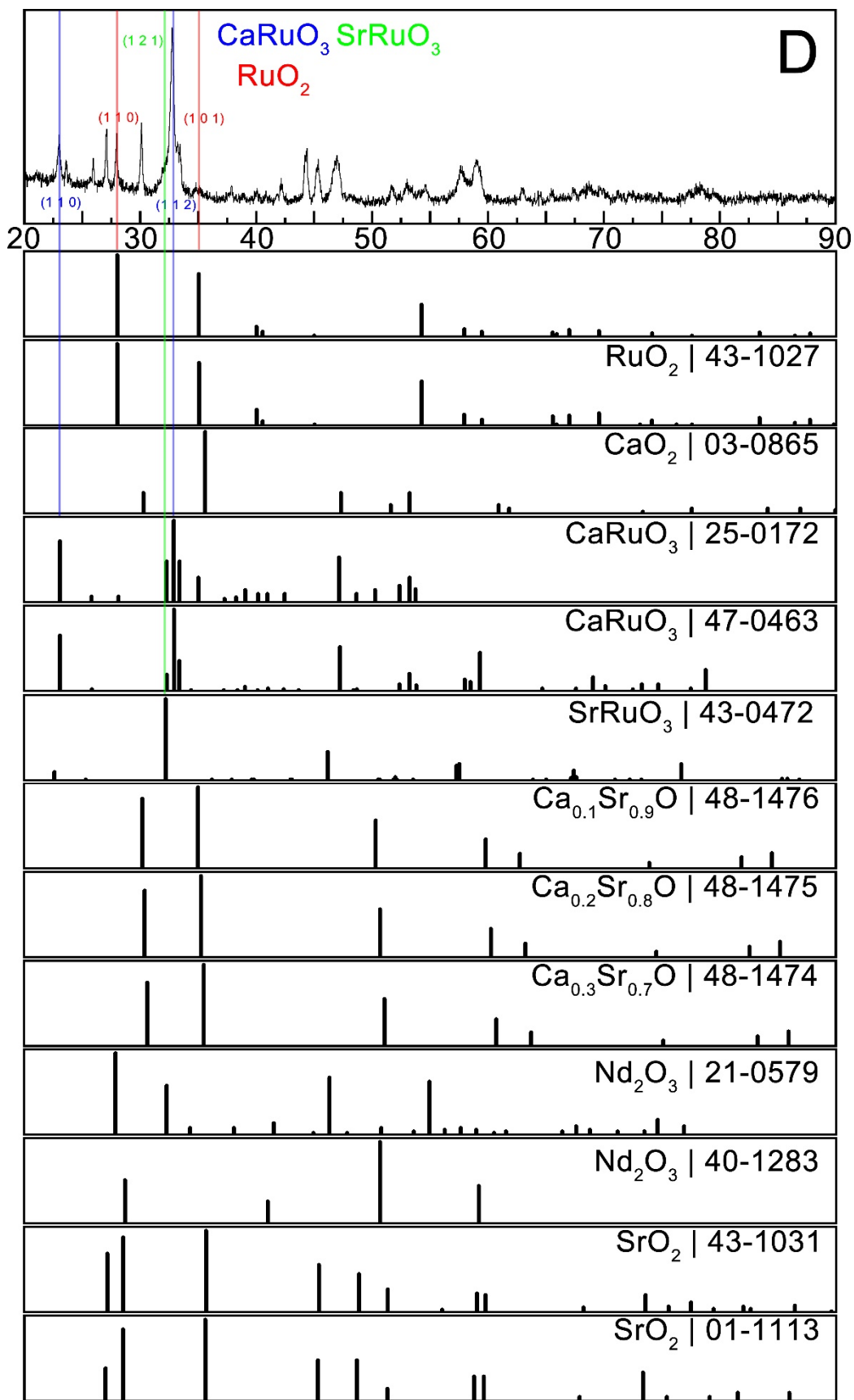


**Fig. SN 5-26** XRD spectra of sample D. Due to complexity and multiple possibilities of existing phases, we only label the dominant peaks and corresponding phases' major facets.

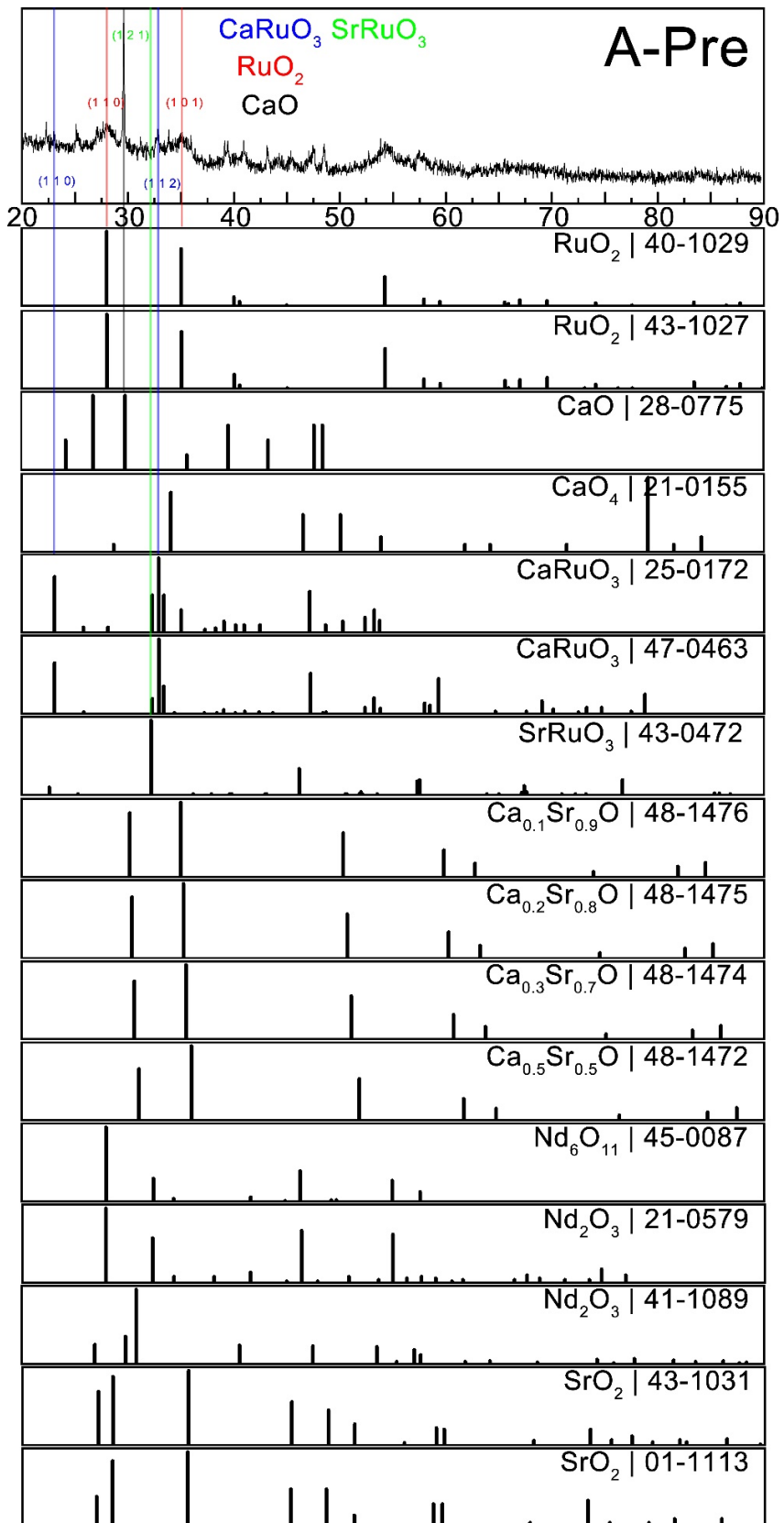


**Fig. SN 5-27** XRD spectra of sample A-Pre. Due to complexity and multiple possibilities of existing phases, we only label the dominant peaks and corresponding phases' major facets.

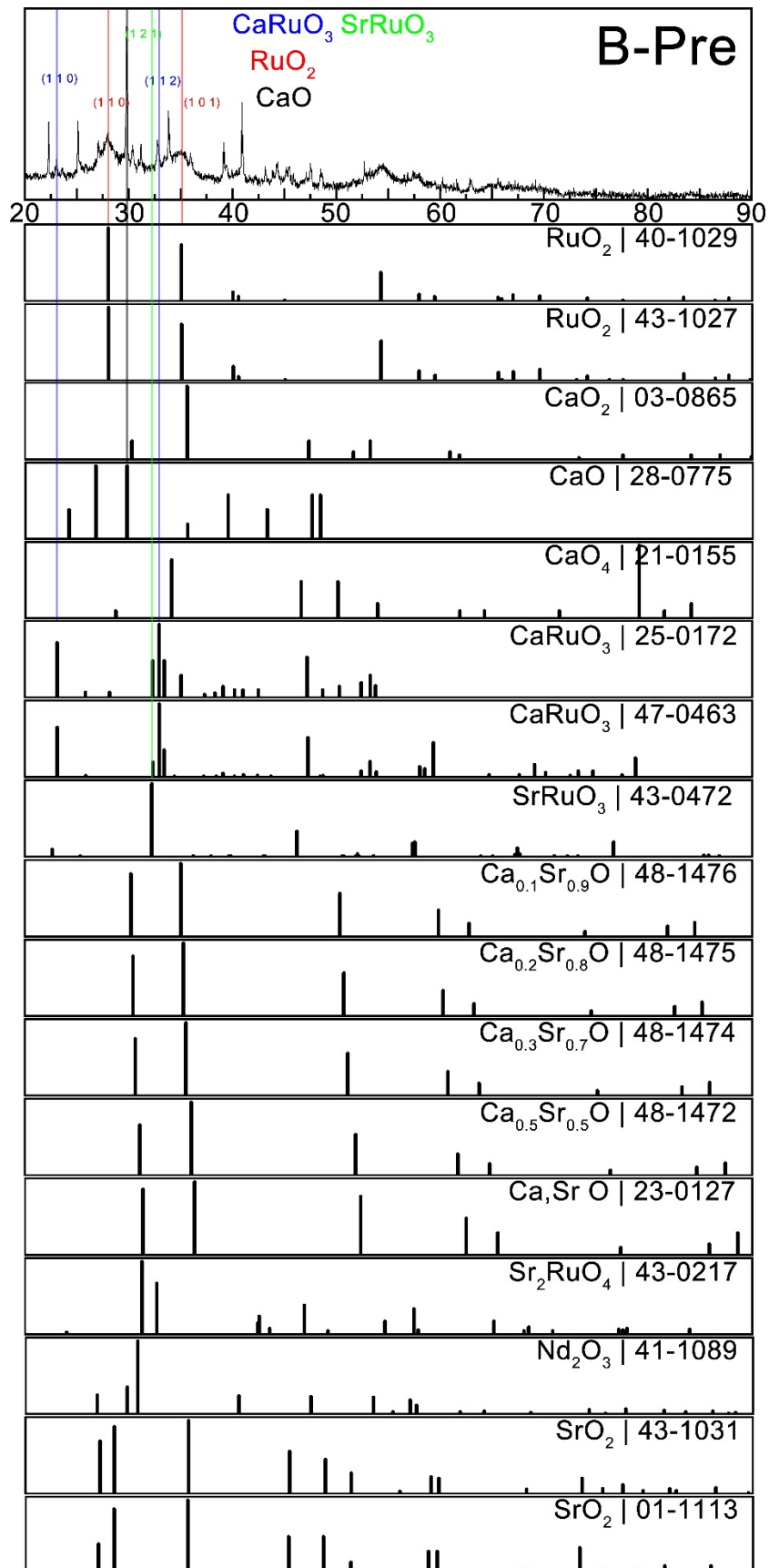


**Fig. SN 5-28** XRD spectra of sample B-Pre. Due to complexity and multiple possibilities of existing phases, we only label the dominant peaks and corresponding phases' major facets.

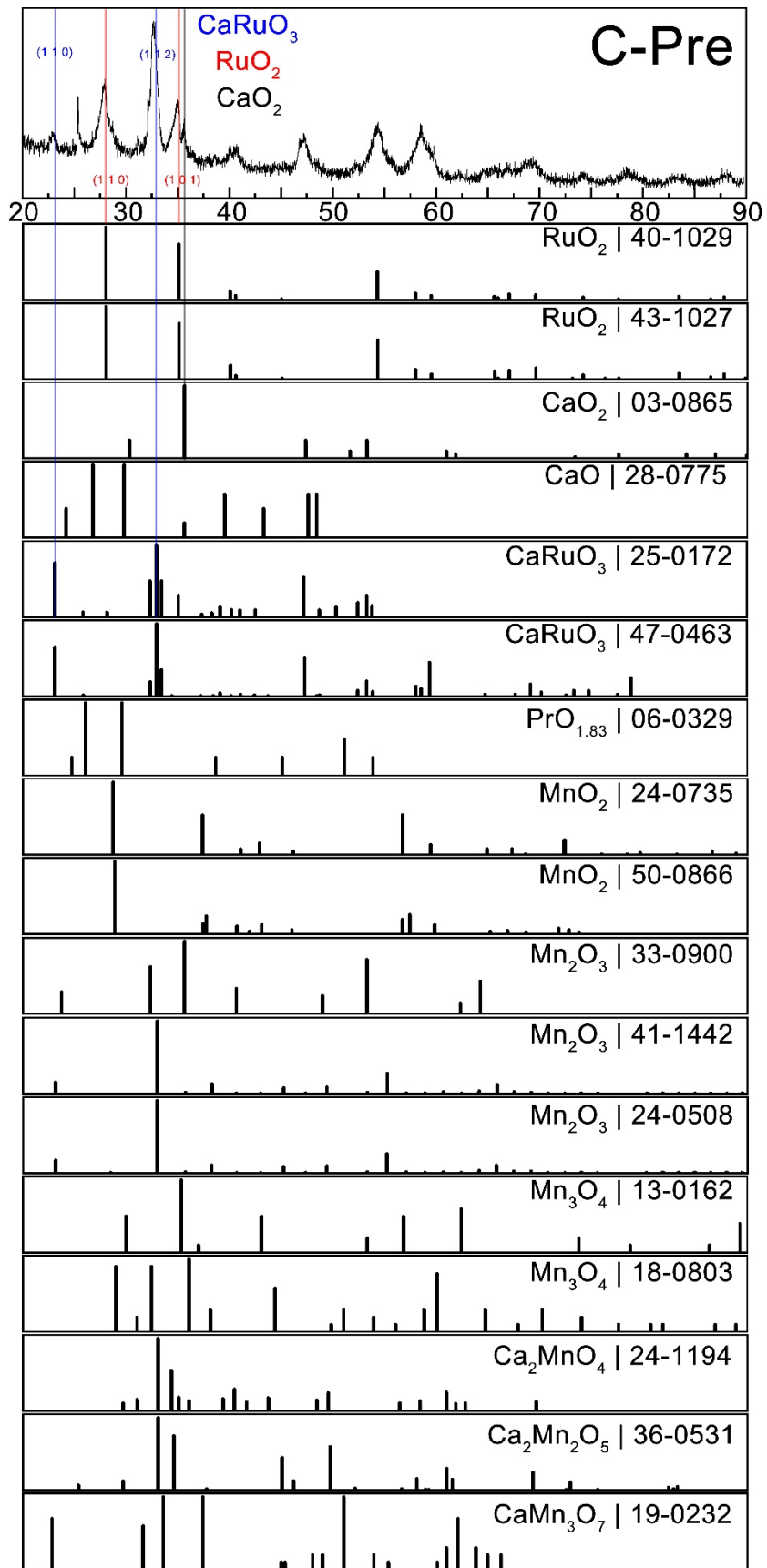


**Fig. SN 5-29** XRD spectra of sample C-Pre. Due to complexity and multiple possibilities of existing phases, we only label the dominant peaks and corresponding phases' major facets.

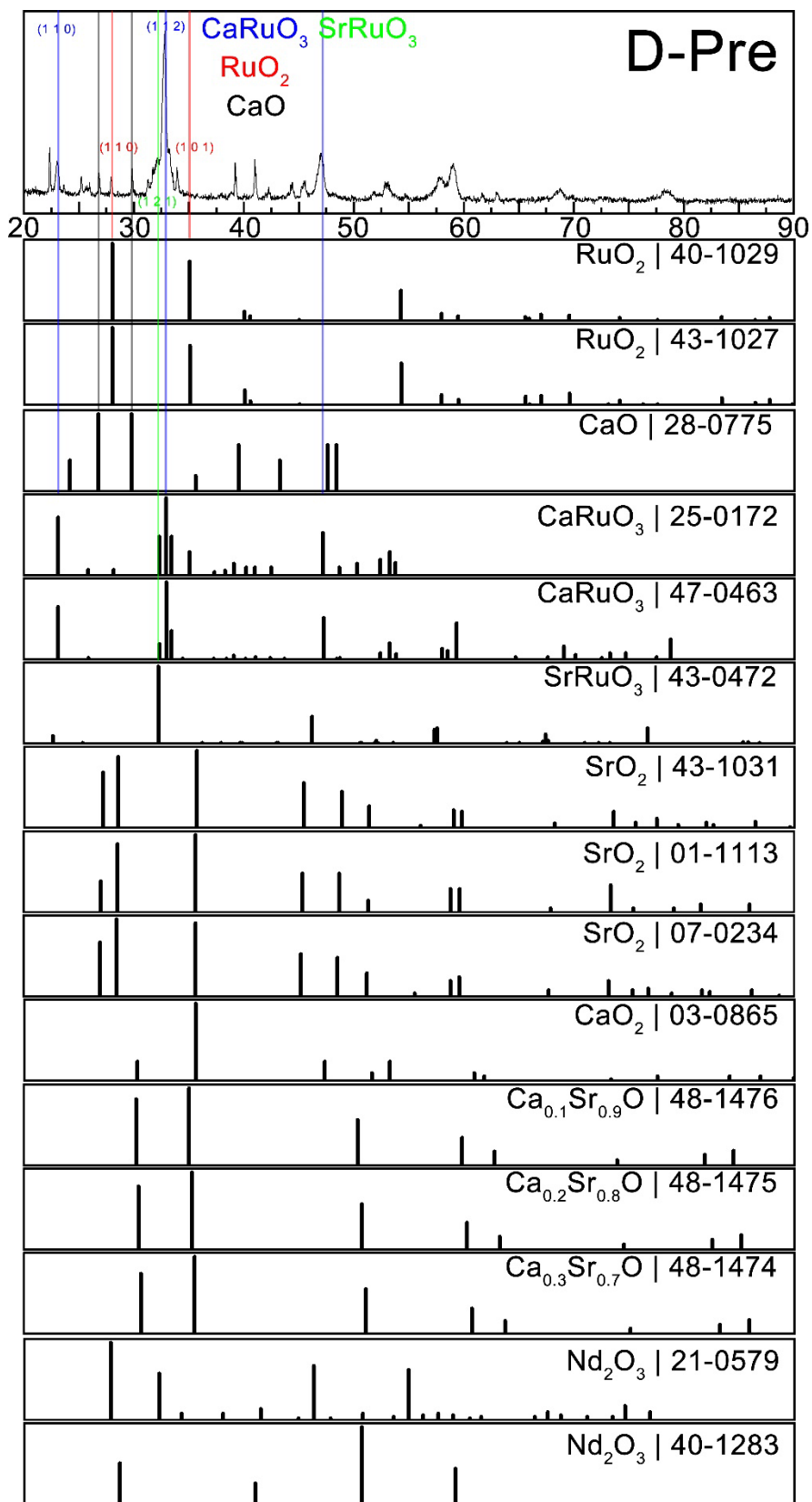


**Fig. SN 5-30** XRD spectra of sample D-Pre. Due to complexity and multiple possibilities of existing phases, we only label the dominant peaks and corresponding phases' major facets.

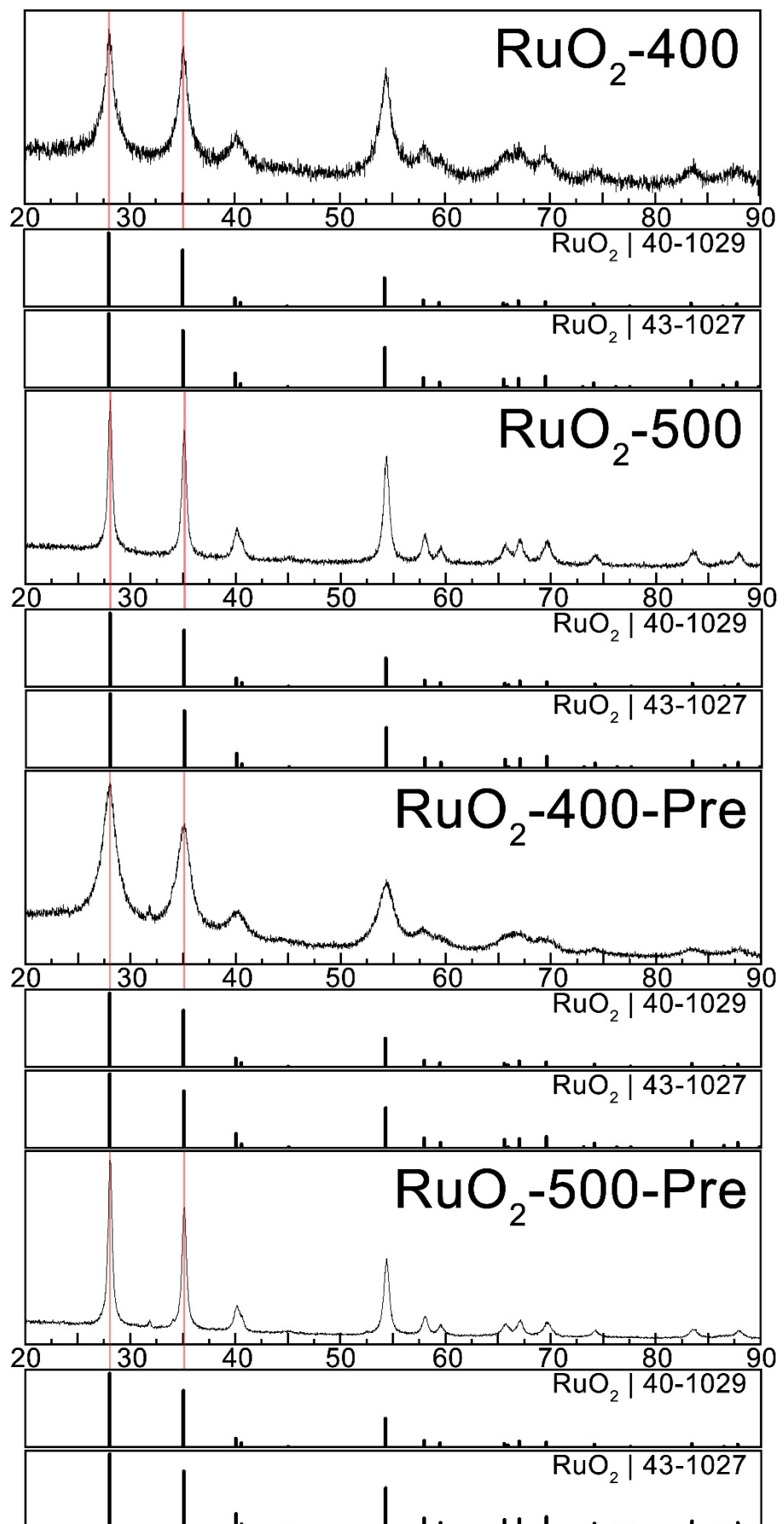


**Fig. SN 5-31** XRD spectra of pure Ru oxide samples.

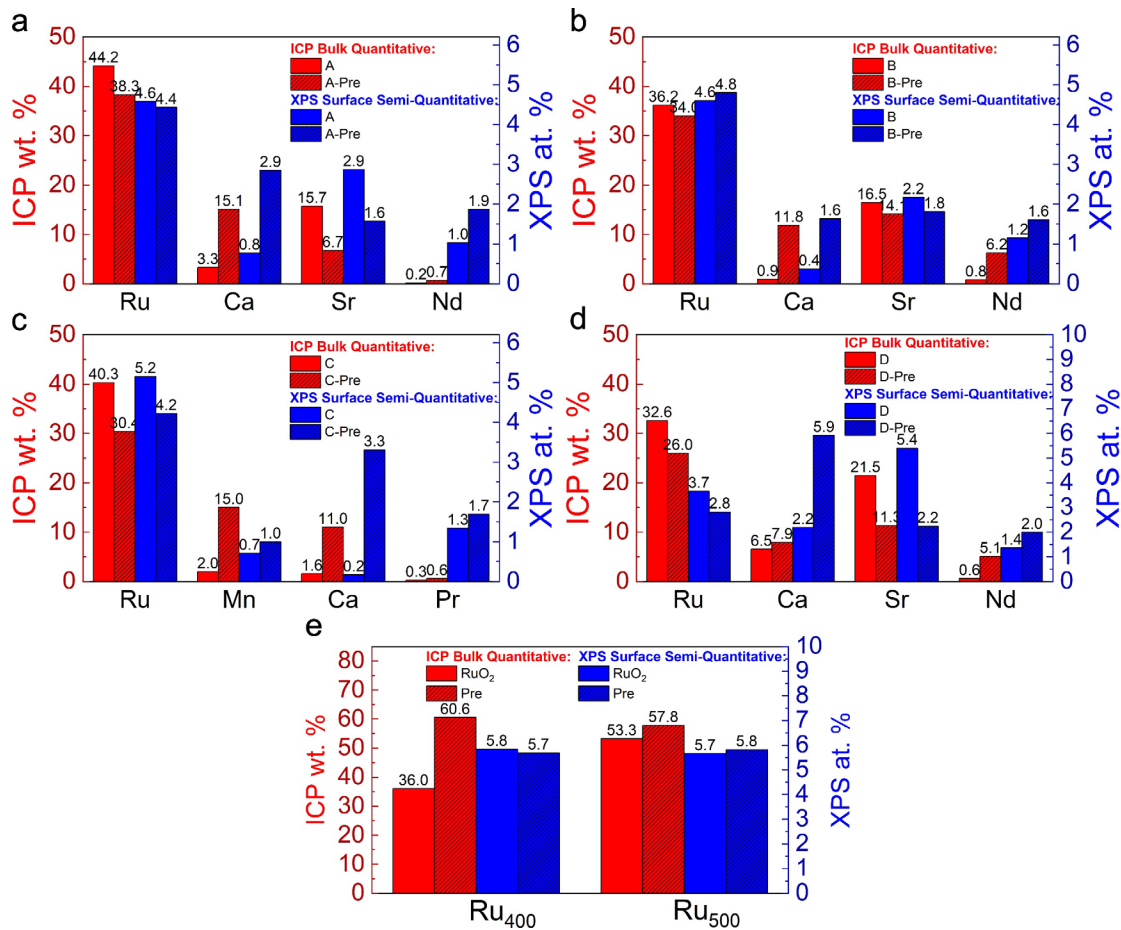


**Fig. SN 5-32 (a)-(e)** The bar chart showing the quantitative bulk mass fractions of various metal elements in 12 different samples obtained through ICP testing, and the semi-quantitative surface atomic fractions derived from XPS spectra.

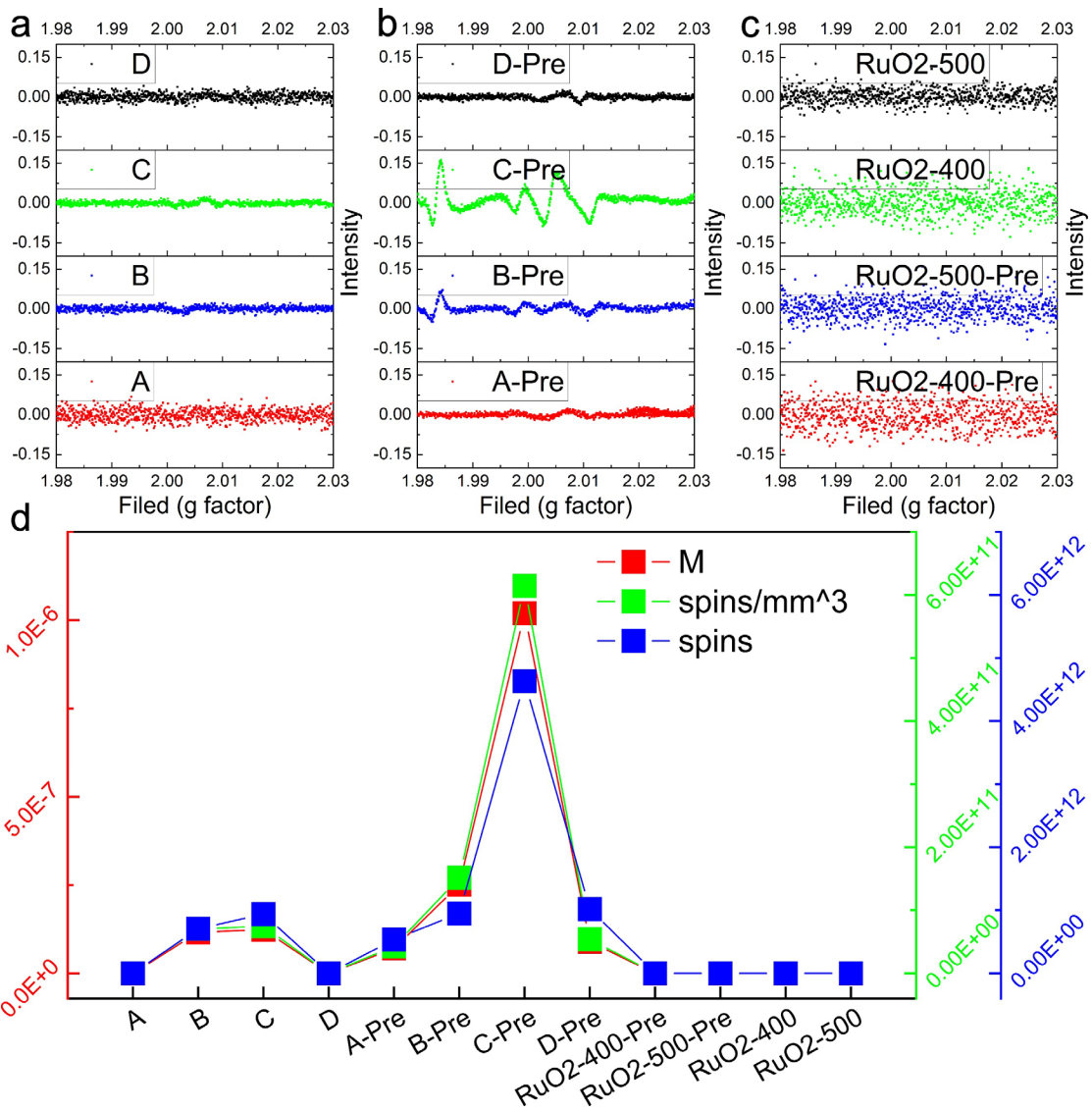


**Fig. SN 5-33** (a)-(c) EPR spectra of 12 different samples, with the g-factor as the horizontal axis; (d) Statistical line graph of magnetic susceptibility (M), in terms of total spins, spins per cubic millimeter (spins/mm<sup>3</sup>), for different samples.

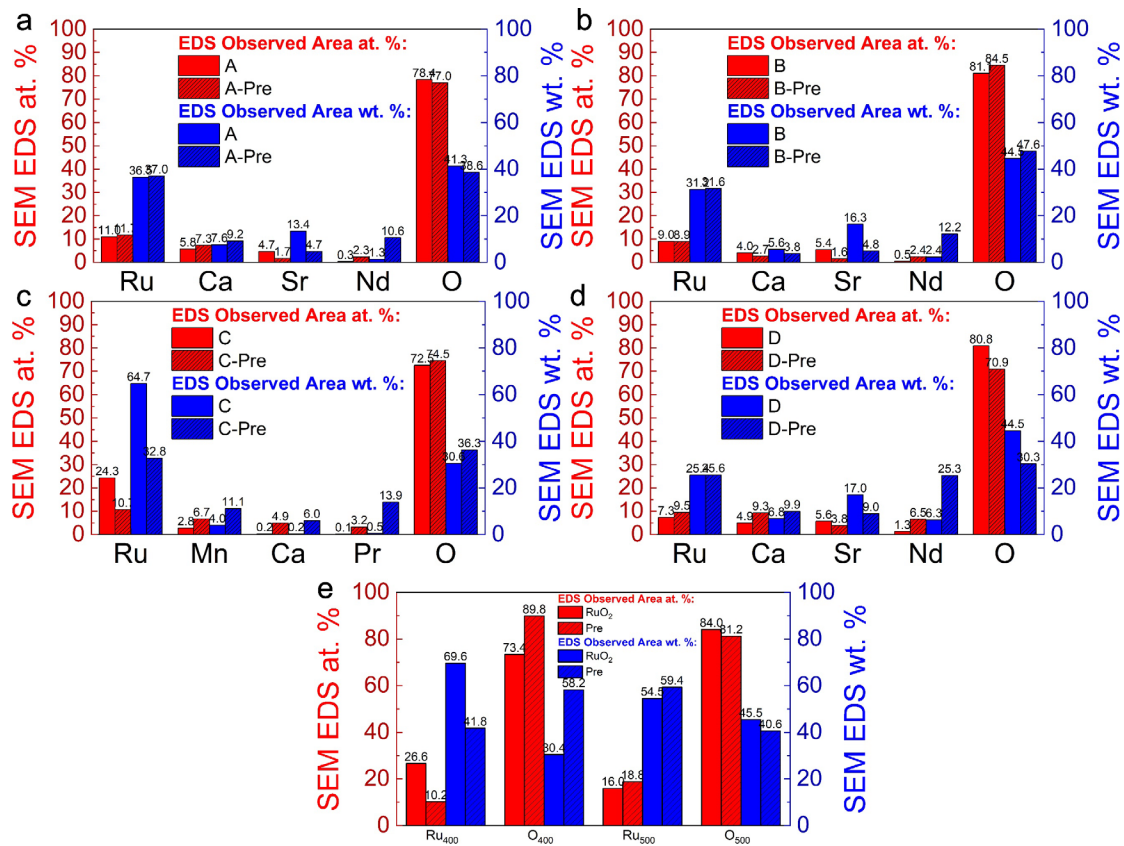


**Fig. SN 5-34 (a)-(e)** The bar chart displaying the atomic and mass fractions of various metal elements (including oxygen in this chart) in 12 different samples, obtained through statistical analysis of SEM-EDX signals.

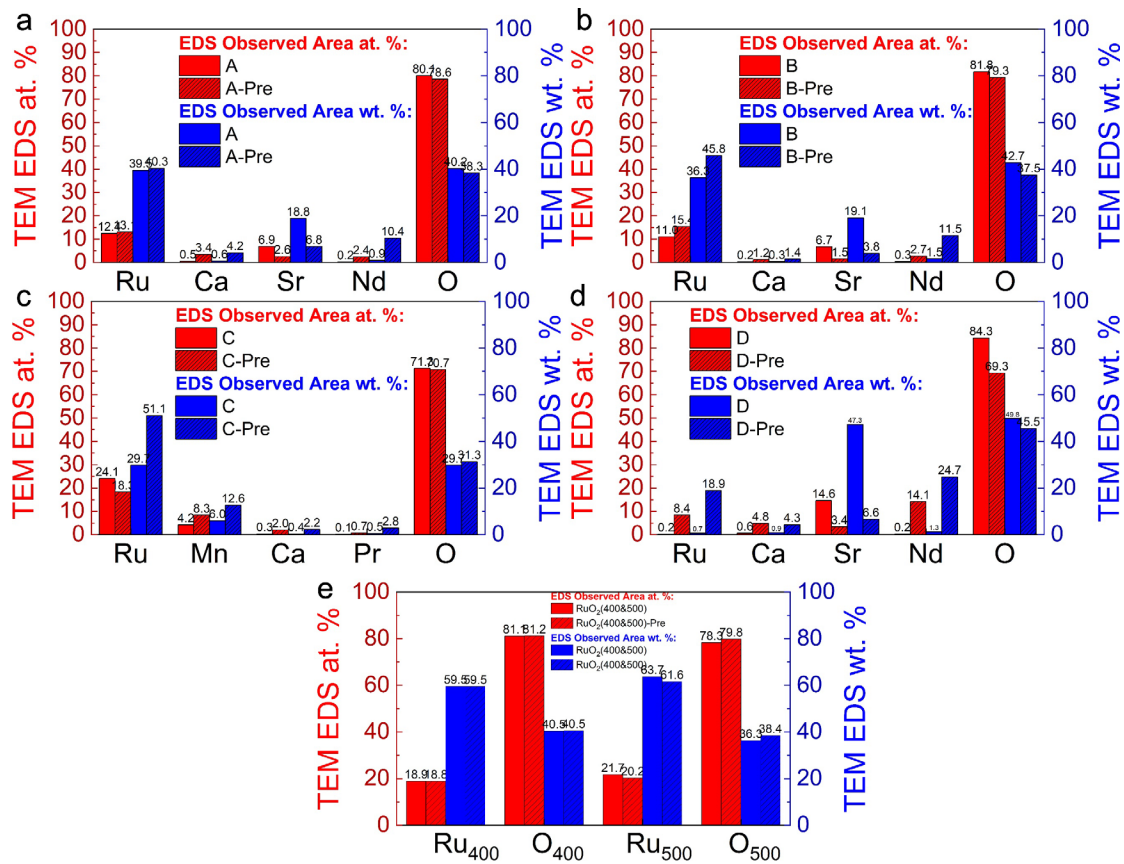


**Fig. SN 5-35 (a)-(e)** The bar chart displaying the atomic and mass fractions of various metal analysis of TEM-EDX signals. elements (including oxygen in this chart) in 12 different samples, obtained through statistical analysis of TEM-EDX signals.

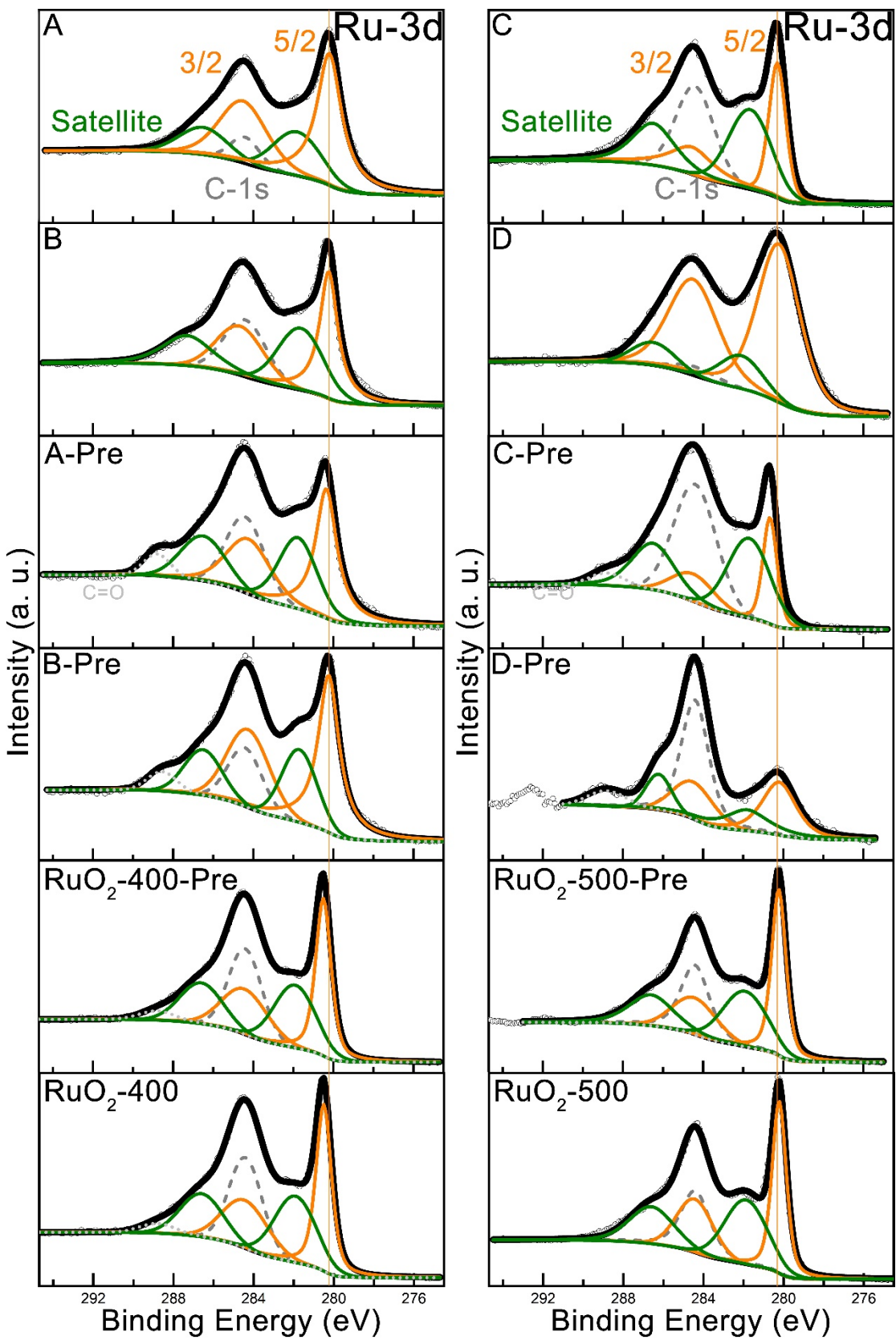


**Fig. SN 5-36** XPS spectra of Ru 3d for different samples.

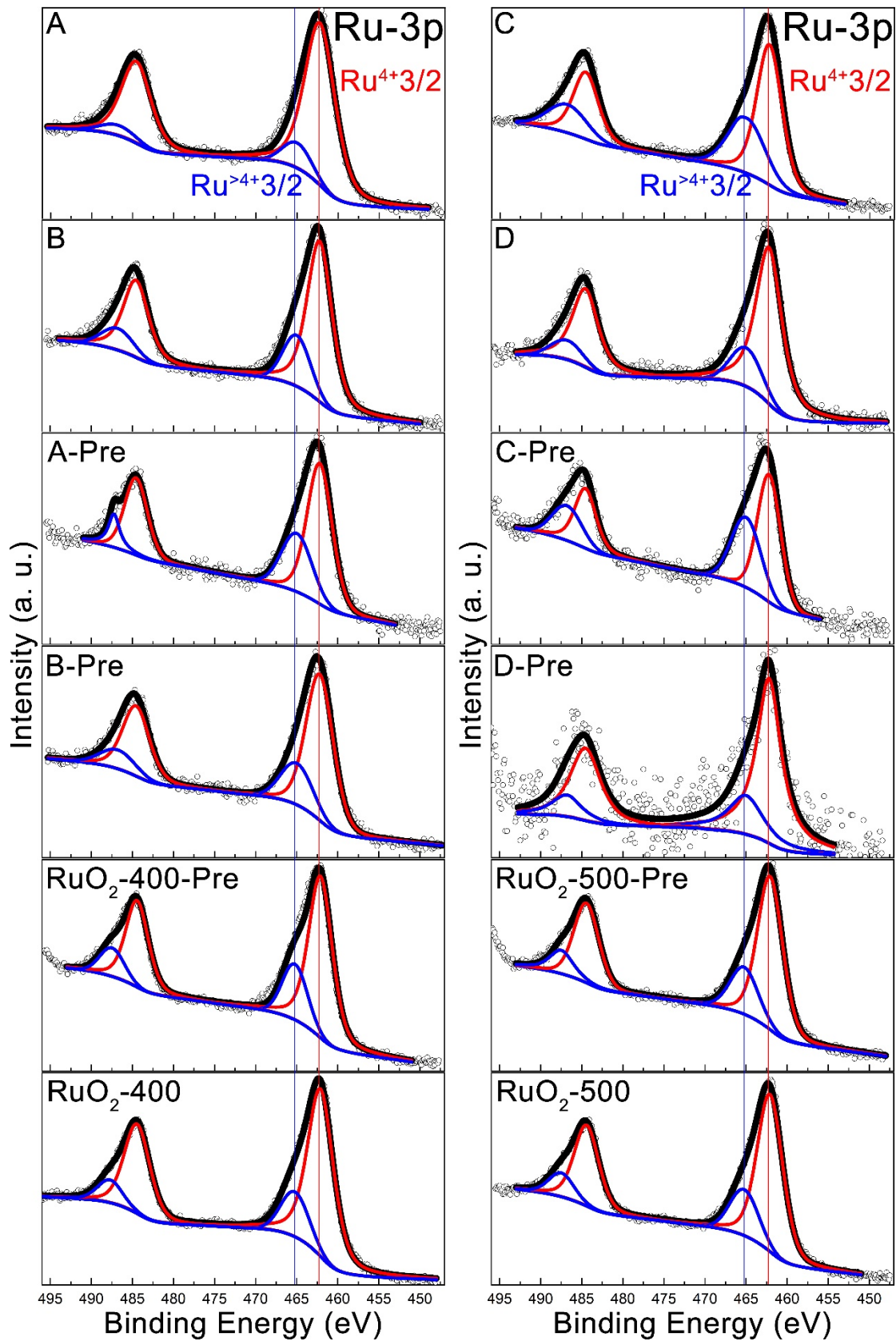


**Fig. SN 5-37** XPS spectra of Ru 3p for different samples.

### **Supplementary Note 5 References:**

1. Rodríguez-García I, Galyamin D, Pascual L, Ferrer P, Peña MA, Grinter D, *et al.* Enhanced stability of SrRuO<sub>3</sub> mixed oxide via monovalent doping in Sr<sub>1-x</sub>K<sub>x</sub>RuO<sub>3</sub> for the oxygen evolution reaction. *Journal of Power Sources* 2022, **521**.
2. Zhang N, Wang C, Chen J, Hu C, Ma J, Deng X, *et al.* Metal Substitution Steering Electron Correlations in Pyrochlore Ruthenates for Efficient Acidic Water Oxidation. *ACS Nano* 2021, **15**(5): 8537-8548.
3. Kim B-J, Abbott DF, Cheng X, Fabbri E, Nachtegaal M, Bozza F, *et al.* Unraveling Thermodynamics, Stability, and Oxygen Evolution Activity of Strontium Ruthenium Perovskite Oxide. *ACS Catalysis* 2017, **7**(5): 3245-3256.
4. Retuerto M, Pascual L, Calle-Vallejo F, Ferrer P, Gianolio D, Pereira AG, *et al.* Na-doped ruthenium perovskite electrocatalysts with improved oxygen evolution activity and durability in acidic media. *Nat Commun* 2019, **10**(1): 2041.
5. Ji M, Yang X, Chang S, Chen W, Wang J, He D, *et al.* RuO<sub>2</sub> clusters derived from bulk SrRuO<sub>3</sub>: Robust catalyst for oxygen evolution reaction in acid. *Nano Research* 2021, **15**(3): 1959-1965.
6. Wang K, Wang Y, Yang B, Li Z, Qin X, Zhang Q, *et al.* Highly active ruthenium sites stabilized by modulating electron-feeding for sustainable acidic oxygen-evolution electrocatalysis. *Energy & Environmental Science* 2022, **15**(6): 2356-2365.